

# Multi-scale semi-supervised clustering of brain images: deriving disease subtypes

Junhao Wen<sup>1,\*</sup>, Erdem Varol<sup>2</sup>, Aristeidis Sotiras<sup>3</sup>, Zhijian Yang<sup>1</sup>, Ganesh B. Chand<sup>4</sup>, Guray Erus<sup>1</sup>, Haochang Shou<sup>1,5</sup>, Gyujoon Hwang<sup>1</sup>, for the Alzheimer's Disease Neuroimaging Initiative<sup>1</sup> and Christos Davatzikos<sup>1,\*</sup>

<sup>1</sup>Center for Biomedical Image Computing and Analytics, Perelman School of Medicine, University of Pennsylvania, Philadelphia, USA

<sup>2</sup>Department of Statistics, Center for Theoretical Neuroscience, Zuckerman Institute, Columbia University, New York, USA

<sup>3</sup>Department of Radiology and Institute for Informatics, Washington University School of Medicine, St. Louis, USA

<sup>4</sup>Department of Radiology, Mallinckrodt Institute of Radiology, Washington University School of Medicine, St. Louis, USA

<sup>5</sup>Penn Statistics in Imaging and Visualization Center, Department of Biostatistics, Epidemiology, and Informatics, Perelman School of Medicine, University of Pennsylvania, Philadelphia, USA

\*Corresponding authors:

Junhao Wen, PhD – [junhao.wen89@gmail.com](mailto:junhao.wen89@gmail.com)

Christos Davatzikos, PhD – [Christos.Davatzikos@pennmedicine.upenn.edu](mailto:Christos.Davatzikos@pennmedicine.upenn.edu)

3700 Hamilton Walk, Philadelphia, PA 19104

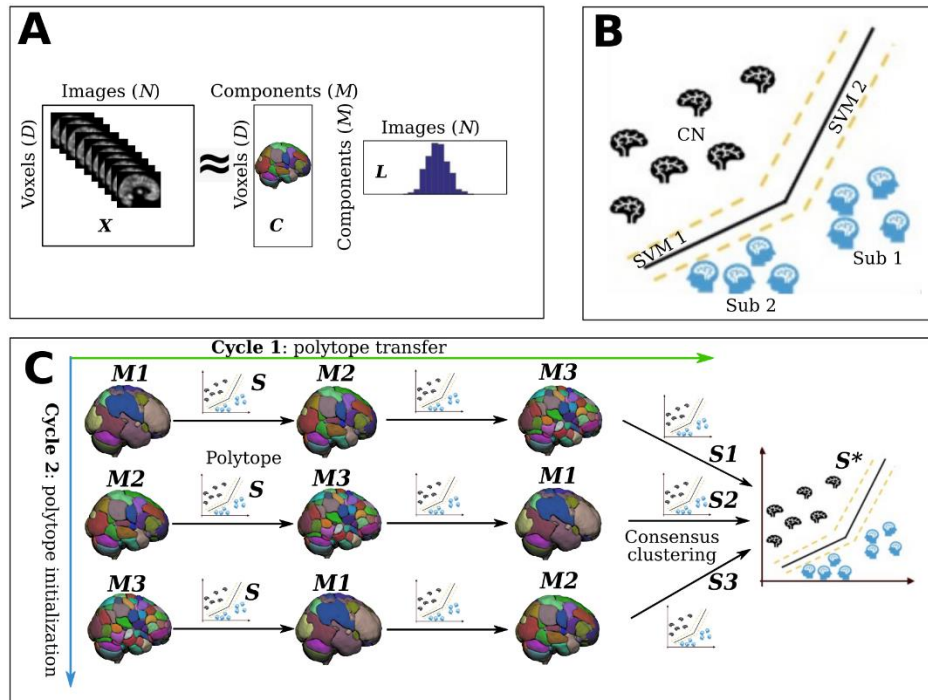
---

<sup>1</sup> Data used in preparation of this article were obtained from the Alzheimer's Disease Neuroimaging Initiative (ADNI) database ([adni.loni.usc.edu](http://adni.loni.usc.edu)). As such, the investigators within the ADNI contributed to the design and implementation of ADNI and/or provided data but did not participate in analysis or writing of this report. A complete listing of ADNI investigators can be found at: [http://adni.loni.usc.edu/wp-content/uploads/how\\_to\\_apply/ADNI\\_Acknowledgement\\_List.pdf](http://adni.loni.usc.edu/wp-content/uploads/how_to_apply/ADNI_Acknowledgement_List.pdf)

## Highlights

- We propose a novel multi-scale semi-supervised clustering method, termed MAGIC, aiming at disentangling the heterogeneity of brain diseases.
- We perform extensive experiments on large control samples (UK Biobank,  $N=4403$ ) to precisely quantify performance under various conditions, including varying degrees of brain atrophy, different levels of heterogeneity, overlapping disease subtypes, class imbalance, and varying sample sizes.
- We demonstrate the strengths of MAGIC relative to other standard clustering methods.
- We apply MAGIC to MCI and Alzheimer's disease datasets (ADNI,  $N=1728$ ) to dissect neuroanatomical heterogeneity in AD and its prodromal stages.

## Graphical abstract



(A) Multi-scale image decomposition using structural covariance analysis via opNMF;  
(B) Convex polytope separates patients from controls, thereby capturing disease subtypes;  
(C) Inter-scale consistent clustering of disease patterns.

## Table of Abbreviations

Item	Abbreviation
Alzheimer's disease	AD
Grey matter	GM
Mild cognitive impairment	MCI
Healthy control	CN
Machine learning	ML
Adjusted Rand index	ARI
Atrophy strength level	ASL
Patients	PT
Subtype	Sub
Cross-validation	CV
Quality control	QC
ARIs during CV	ARI_CV
ARIs for ground truth	ARI_GT
T1-weighted MRI	T1w MRI
Magnetic resonance imaging	MRI
Non-negative matrix factorization	NMF
Voxel-based analysis	VBA
Multivariate pattern analysis	MVPA
Support vector machine	SVM

## Table of variables

Item	Abbreviation
Number of clusters/subtypes	$k$
Number of components	$M$
Number of subjects	$N$
Number of voxels	$D$
Input matrix	$X$
Component matrix	$C$
Loading coefficient matrix	$L$
Input label	$y$
SVM weight	$w$
SVM bias	$b$
Subtype membership matrix	$S$
Final subtype membership matrix after consensus clustering	$S^*$
Index of number of subjects	$i$
Index of number of clusters/subtypes	$j$
Index of number of blocks in cyclic optimization	$q$
Total number blocks in cyclic optimization	$Q$

## Abstract

Disease heterogeneity is a significant obstacle to understanding pathological processes and delivering precision diagnostics and treatment. Clustering methods have gained popularity in stratifying patients into subpopulations (i.e., subtypes) of brain diseases using imaging data. However, unsupervised clustering approaches are often confounded by anatomical and functional variations not related to a disease or pathology of interest. Semi-supervised clustering techniques have been proposed to overcome this and, therefore, capture disease-specific patterns more effectively. An additional limitation of both unsupervised and semi-supervised conventional machine learning methods is that they typically model, learn and infer from data at a basis of feature sets pre-defined at a fixed scale or scales (e.g, an atlas-based regions of interest). Herein we propose a novel method, “Multi-scale heterogeneity analysis and Clustering” (MAGIC), to depict the multi-scale presentation of disease heterogeneity, which builds on a previously proposed semi-supervised clustering method, HYDRA. It derives multi-scale and clinically interpretable feature representations and exploits a double-cyclic optimization procedure to drive inter-scale-consistent disease subtypes or neuroanatomical dimensions effectively. More importantly, to fill in the gap of understanding under what conditions the clustering model can estimate true heterogeneity related to diseases, we conducted extensive and systematic semi-simulated experiments to evaluate the proposed method on a sizeable healthy control sample from the UK Biobank (N=4403). We then applied MAGIC to real imaging data of Alzheimer’s disease (ADNI, N=1728) to demonstrate its potential and challenges in dissecting the neuroanatomical heterogeneity of brain diseases. Taken together, we aim to provide guidelines on when such analyses can succeed or should be taken with caution. The code of the proposed method is publicly available at <https://github.com/anbai106/MAGIC>.

**Keywords:** semi-supervised, clustering, multi-scale, heterogeneity, semi-simulated

## 1. Introduction

Statistical and machine learning (ML) methods have been widely applied to neuroimaging data to derive disease-specific imaging signatures (Davatzikos, 2019). Voxel-based analysis (VBA) techniques generally involve performing independent mass univariate statistical tests on all voxels (Ashburner et al., 1998; Ashburner and Friston, 2000; Davatzikos et al., 2001; Friston et al., 1994), aiming to unveil detailed spatial maps of brain structures that are associated with clinical variables of interest. However, VBA approaches suffer from limited statistical power since they ignore multivariate data interactions. In contrast, multivariate pattern analysis (MVPA) techniques have gained traction due to their ability to capture complex multivariate interactions in data. Classical multivariate models, such as support vector machine (SVM), have been extensively utilized in the neuroimaging community to reveal imaging signatures for several brain diseases and disorders (Cuingnet et al., 2011; Ecker et al., 2010; Gaonkar and Davatzikos, 2013; Habes et al., 2016; Koutsouleris et al., 2015; Lao et al., 2004; Rathore et al., 2017; Samper-González et al., 2018; Varol et al., 2018). More recently, highly nonlinear and multivariate deep learning models have also been applied to brain modeling (Bashyam et al., 2020; Schulz et al., 2020; Wen et al., 2020a). However, due to possible over-fitting, these models' interpretability and generalizability in low sample size regimes have been under scrutiny.

Whether performing mass univariate or multivariate analysis, it is typically assumed that a relatively pure pathological pattern exists in the disease population. The disease signature is often presented via a voxel-wise or region of interest (ROI)-wise statistical map of the case-control group differences, i.e., between healthy controls (CN) and patients (PT). However, in nature, disease effects are commonly heterogeneously presented across different subpopulations due to the diversity of underlying risk factors. Such model assumption violations may cause the statistical learning to yield underpowered or false-positive results (Dwyer et al., 2018). Tackling this issue is of great importance given ample evidence of disease heterogeneity (Murray et al., 2011; Noh et al., 2014; Whitwell et al., 2007) and increasing appreciation that this may undermine the precision of clinical treatment guidelines and obscure research findings (Insel and Cuthbert, 2015).

Disentangling disease heterogeneity elucidates the underlying pathological mechanisms and potentially enables clinicians to offer targeted treatment options to different patient subpopulations. Nonlinear methods, such as deep neural networks, implicitly handle heterogeneity. However, there still exists a gap between these models and human interpretability, especially for clinicians who frequently seek discrete disease subtypes (Miotto et al., 2018). Thus, many recent efforts to discover the heterogeneous nature of brain diseases have investigated different clustering algorithms (Chand et al., 2020; Dong et al., 2016a, 2016b; Dwyer et al., 2018; Ezzati et al., 2020; Filipovych et al., 2012; Honnorat et al., 2019; Jeon et al., 2019; Jung et al., 2016; Lubeiro et al., 2016; Nettiksimmons et al., 2014; Ota et al., 2016; Pan et al., 2020; Park et al., 2017; Planchuelo-Gómez et al., 2020; Poulakis et al., 2020, 2020, 2018; Sugihara et al., 2016; Ten Kate et al., 2018; Varol et al., 2017; Young et al., 2018; Zhang et al., 2016). These methods can be divided into two categories depending on whether the clustering algorithm is unsupervised or semi-supervised<sup>2</sup>. Unsupervised clustering techniques, such as K-means (Hartigan and Wong, 1979), hierarchical clustering (Day and Edelsbrunner, 1984), and non-negative matrix factorization (NMF) (Lee and Seung, 2001), aim to directly cluster the patients based on their demographic information, clinical presentation, or imaging biomarkers. However, the results of these methods have often been confounded by non-pathologic processes, such as demographics. To cope with these covariate confounds semi-supervised clustering methods (Dong et al., 2016a; Varol et al., 2017) leverage the group-level information and attempt to nullify the effect of nuisance variables. These methods generate clusters based on the pattern differences between the CN population and the subpopulations of patients (i.e., subtypes/clusters), hypothesizing that each pattern represents a distinct disease dimension or subtype. The main limitation of this family of methods is that they usually seek subtypes on a single scale set of features (e.g., atlas-based ROIs, voxels, networks), which makes the result heavily dependent on the level of granularity of the feature space. However, there has been abundant evidence that the brain is fundamentally constructed by multi-scale entities (Bassett and Siebenhühner, 2013; Betzel and Bassett, 2017). Therefore, it is beneficial to analyze disease heterogeneity on multiple spatial scales and seek a clustering solution that is compatible across scales, which will potentially better align with the brain's multi-scale nature.

---

<sup>2</sup> The term semi-supervised refers to the lack of subtype labels and the use of CN as a reference group to guide the clustering.

Despite that these clustering works have always led to a cluster solution, guidelines enabling the validity of the cluster solution claimed have yet to be established, presumably due to the lack of the ground truth in clustering problems or the “curse of dimensionality” in brain imaging settings. A previous study (Varol et al., 2017) designed simulation experiments to validate the proposed model. However, the simulation data were generated by adding noise in the low-dimensional feature space under a specific distribution (i.e., Gaussian distribution), which was far less realistic than actual neuroimaging data. Thus, a more sophisticated and systematic simulation is needed to understand at what conditions clustering succeeds or fails with high-dimensional brain imaging data. Specifically, in the current work, we performed an extensive and systematic evaluation on clustering performance using a large healthy control sample (UK Biobank,  $N=4403$ ) in a semi-simulated setting. The term semi-simulated is in reference to the fact that the disease effects (e.g., brain atrophy) are imposed on specific regions of tissue images of real healthy control individuals. With known ground truth for the number of clusters ( $k$ ) and the cluster/subtype membership assignment, we quantitatively investigated the clustering model’s performance under a variety of conditions, including varying degrees of brain atrophy, different levels of heterogeneity, overlapping disease subtypes, class imbalance, and varying sample sizes.

This work is a comprehensive extension of our preliminary results presented in Medical Image Computing and Computer Assisted Interventions (MICCAI) in 2020 (Wen et al., 2020b). The contribution is two-fold. First, to address the aforementioned multi-scale limitations, we propose a data-driven and multi-scale semi-supervised method termed MAGIC for “Multi-scAle heteroGeneity analysIs and Clustering”. Specifically, MAGIC extracts multi-scale features, from coarse to fine granularity, via orthogonal projective non-negative matrix factorization (opNMF) applied for varying scales (i.e., number of components). opNMF has been a very effective unbiased, data-driven method for extracting biologically interpretable and reproducible feature representations in the context of neuroimaging datasets (Sotiras et al., 2015). A convex polytope classifier, based on principles of the method in (Varol et al., 2017), is applied to these multi-scale features through a double-cyclic optimization procedure to yield robust clusters that are consistent across different scales. Secondly, the results of our semi-simulated experiments are of great value. They allow us to compare MAGIC with previous standard clustering methods and provide future clustering analysis guidelines. Subsequently, applying MAGIC to Alzheimer’s disease (AD) and mild cognitive impairment (MCI) patients shows the potential of the proposed model and challenges in clinical application.

We organize the remainder of the paper as follows. In Section 2, we provide the details of the proposed algorithm. Section 3 details the primary datasets and image preprocessing steps. Section 4 presents the results of the experiments. Section 5 concludes the paper by discussing our main observations, method limitations, and future directions.

## 2. Methods

MAGIC builds upon the HYDRA formulation (Varol et al., 2017) and opNMF algorithms (Sotiras et al., 2015) to yield an inter-scale-consistent clustering solution. It generates an interpretable and spatially adaptive multi-scale representation via opNMF, which drives semi-supervised clustering. The schematic diagram of MAGIC is shown in Fig. 1.

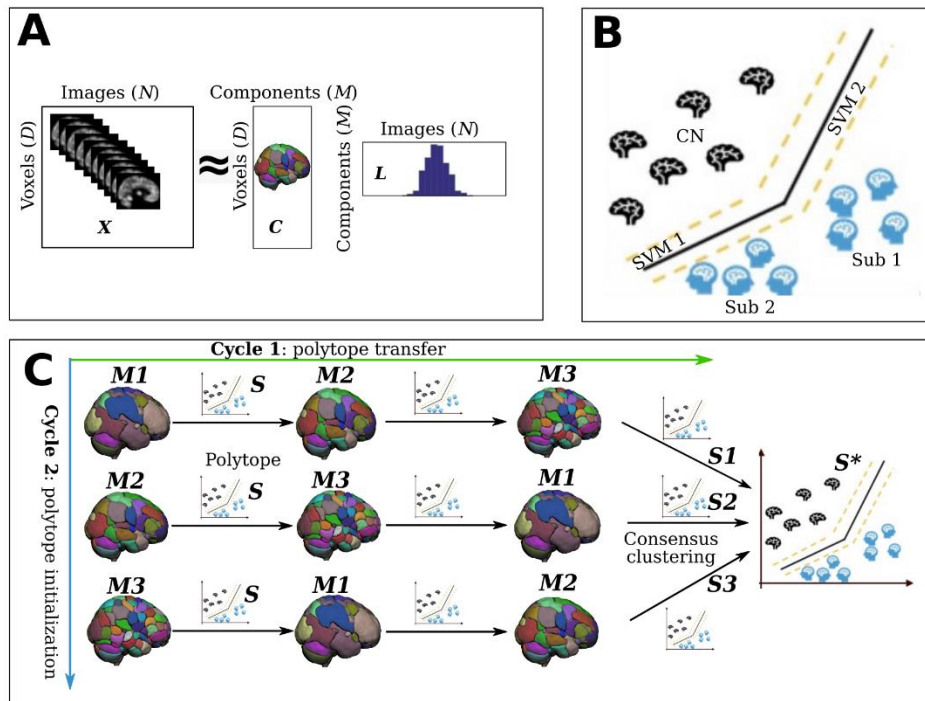


**Figure 1.** Schematic diagram of the MAGIC algorithm. MAGIC first generates multi-scale feature representations of the brain anatomy from coarse to fine resolutions and then cyclically solves semi-supervised clustering subproblems with each of these feature representations. Generally, it consists of three key components. A) opNMF enables the extraction of multi-scale, biologically interpretable feature representations in a data-driven manner. B) max-margin multiple SVM classifiers are utilized to construct a nonlinear polytope for simultaneous classification and clustering. In this fashion, the patients' subtypes or subpopulations are clustered based on their distance from the polytope. C) the double-cyclic optimization procedure is adopted to fuse the knowledge from multi-scale features for inter-scale consistent clustering solutions. Specifically, the cluster polytope is first initialized at a specific representation scale. After optimization, the cluster polytope is transferred to the next representation scale, allowing the clustering routine to be guided by all anatomical scales. Furthermore, the polytope initialization is performed at different anatomical scales to further remove bias from the clustering solutions. Lastly, the resulting multi-scale clustering solutions are fused through consensus clustering to yield a final stable subtype membership assignment.  $X$ : input matrix;  $C$ : component matrix;  $L$ : loading coefficient matrix; CN: healthy control; Sub: subtype;  $M$ : number of components.  $S$  is the initial polytope solution.  $S1$ ,  $S2$ , and  $S3$  are the fine-tuned polytope for different initialization models, and  $S^*$  is the final polytope after consensus clustering procedure.

We detail the mathematical formulation of the optimization routine in the following subsections. To establish notation, let  $N$  denote the number of subjects and  $D$  the number of voxels in each image. We denote the data as a matrix  $X$  that is organized by arranging each image as a vector per column ( $X = [x_1, \dots, x_N]$ ,  $x_i \in R^D$ ). We use binary labels to distinguish the patient and control groups, where 1 represents patients (PT) and -1 means healthy controls (CN) (i.e.,  $y \in \{-1, 1\}^N$ ). For subtype results, the subtype membership matrix (a.k.a., polytope) is denoted as  $S \in R^{N \times k}$  before consensus clustering and  $S^*$  as the final subtype membership matrix after consensus clustering.



## 2.1. Multi-scale feature extraction via orthogonal projective non-negative matrix factorization

MAGIC utilizes opNMF, an unsupervised representation learning algorithm, to extract multi-scale and interpretable anatomical components covering the whole brain. The number of components ( $M$ ) is optimized in opNMF and controls the granularity of the anatomical components (e.g., opNMF components at different granularities can be seen in Fig. 1C).

The opNMF aims to represent the input matrix  $X$  as a rank- $M$  matrix that is the product of two non-negative matrices: i)  $C$ , termed as the component matrix, captures the groups of voxels that covary most and offers an interpretable anatomical parcellation ( $C = [c_1, \dots, c_M]$ ,  $c_i \in R^D$ ), and ii)  $L \in R^{M \times N}$ , termed as the loading coefficient matrix, captures the amount of each spatial component that makes up each subject. The opNMF objective is as follows:

$$\min_c \|X - CL\|_F^2 \quad \text{subject to } C \geq 0, L \geq 0, C^T C = I, L = C^T X \quad (1)$$

This formulation differs from the standard NMF since the loading coefficient matrix is obtained by projecting the input data  $X$  to the estimated component matrix  $C$  (i.e.,  $L = C^T X$ ), and the orthogonality constraint is imposed on the component matrix ( $C^T C = I$ , where  $I$  denotes the identity matrix). Therefore, the opNMF searches only the parameters of the component matrix during optimization (Zhirong Yang and Oja, 2010). Once the algorithm converges, we recover the loading coefficients by the projective step:  $L = C^T X$ .

### 2.1.1. Max-margin multiple SVM classifiers for clustering

Once the high dimensional imaging data is reduced to a lower-dimensional representation using opNMF, we apply the HYDRA algorithm (Varol et al., 2017) on the set of loading coefficients,  $L \in R^{M \times N}$  and the corresponding set of diagnostic labels  $y \in \{-1, 1\}^N$  to perform clustering of the patients. In general, this algorithm solves for a convex polytope classification boundary that discriminates patients from controls with maximum margin. In essence, the polytope is composed of the  $k$  hyperplanes of the  $k$  linear SVMs, and each face corresponds to one subtype/cluster. The objective of maximizing the polytope's margin can be summarized as:

$$\min_{\{w_j, b_j\}_{j=1}^k} \sum_{j=1}^k \frac{\|w_j\|_2^2}{2} + \mu \sum_{i|y_i=+1} \frac{1}{k} \max\{0, 1 - w_j^T L_i^T - b_j\} + \mu \sum_{i|y_i=-1} S_{i,j} \max\{0, 1 + w_j^T L_i^T + b_j\} \quad (2)$$

where  $w_j$  and  $b_j$  are the weight and bias for each hyperplane, respectively.  $\mu$  is a penalty parameter on the training error, and  $S$  is the subtype membership matrix of dimension  $N \times K$  containing information regarding whether a sample  $i$  belongs to subtype  $j$ . In general, this optimization problem is non-convex and is jointly optimized by iterating on solving for the polytope faces' parameters using standard SVM solvers (Chang and Lin, 2011) and solving for the cluster memberships as follows:

$$S_{i,j} = \begin{cases} 1, & j = \underset{j}{\operatorname{argmax}}(w_j^T L_i^T + b_j) \\ 0, & j \neq \underset{j}{\operatorname{argmax}}(w_j^T L_i^T + b_j) \end{cases} \quad (3)$$

### 2.1.2. Double-cyclic optimization procedure for scale-independent subtypes

MAGIC optimizes the clustering objective, i.e., Eq. 2, for each anatomical scale as a sub-optimization problem. To fuse the multi-scale clustering solutions and enforce the clusters to be scale-independent, MAGIC adopts a double-cyclic optimization procedure that transfers and fine-tunes the subtype membership matrix ( $S$ ) between different scales of features, i.e., solving the sub-optimization problems with the single-scale feature representation in a loop. Formally, MAGIC solves the overall clustering problem in the form of:

$$\min_{\{\mathbf{S}_q, \mathbf{w}_q, \mathbf{b}_q\}_{q=1}^Q} F\{(\mathbf{S}_1, \mathbf{w}_1, \mathbf{b}_1), \dots, (\mathbf{S}_q, \mathbf{w}_q, \mathbf{b}_q)\} \quad (4)$$

where  $Q \in R$  is the total number of blocks that the optimization takes until the pre-defined stopping criteria achieve.  $(\mathbf{S}_q, \mathbf{w}_q, \mathbf{b}_q)$  are the polytope, weight, and bias terms estimated using the  $q$ -th set of features.

The double-cyclic fine-tuning procedure aims to offer scale-independent clustering solutions across multi-scale features. Cycle 1 (Fig. 1C components  $M1$ ,  $M2$ , and  $M3$  in a row) aims to derive a clustering solution that is informed by features across all scales. This is achieved by iteratively solving Eq. 2 using features derived at different scales. Specifically, the clustering membership matrix  $\mathbf{S}$  is first solved for a particular set of features. It is then transferred to the next block, where it is used as initialization for fine-tuning driven by features from a different scale. This procedure is repeated till features from all anatomical scales have been used to inform the final clustering membership matrix ( $\mathbf{SI}$  in Fig. 1C). Since each optimization cycle starts at a pre-determined anatomical scale, an additional Cycle 2 (Fig. 1C components  $M1$ ,  $M2$ , and  $M3$  in a column) is executed using all different anatomical scales to initialize the model. This eliminates any initialization biases ( $\mathbf{SI}$ ,  $\mathbf{S2}$ , and  $\mathbf{S3}$  in Fig. 1C) and results in multiple clustering solutions. To determine the final subtype assignment ( $\mathbf{S}^*$  in Fig. 1C), we perform consensus clustering. Consensus is achieved by grouping together samples that are assigned to the same cluster across the solutions estimated as part of Cycle 2 (Varol et al., 2017). Specifically, we first compute a co-occurrence matrix based on the clustering results of Cycle 2 and then use it to perform spectral clustering (Ng et al., 2001).

### 3. Materials

#### 3.1. Datasets

The neuroimaging data used in the current study are from three datasets: the UK Biobank (UKBB) study (Miller et al., 2016) and the Alzheimer's Disease Neuroimaging Initiative (ADNI) study (Petersen et al., 2010).

The UKBB is a dataset of approximately 500,000 UK adults sampled via population-based registries (<http://www.ukbiobank.ac.uk>). Participants were recruited from across the United Kingdom, and initial enrolment was carried out from 2006 to 2010. Participants provided socio-demographic, cognitive, and medical data via questionnaires and physical assessments. Starting in 2014, a subset of the original sample later underwent brain magnetic resonance imaging (MRI). The UKBB data used in this work comprises 4403 CN participants whose T1-weighted (T1w) MRI was collected using Siemens 3T Skyra. The parameters of the 3D MPRAGE sequences are as follows: resolution=1.0×1.0×1.0 mm; field-of-view=256 mm x256 mm; TR = 2000 ms; TE = 2.01 ms; TI = 880 ms; slices = 208; flip angle = 8 degrees (Miller et al., 2016).

The ADNI was launched in 2003 as a public-private partnership ([www.adni-info.org](http://www.adni-info.org)). The primary goal of ADNI has been to test whether serial MRI, positron emission tomography (PET), other biological markers, and clinical and neuropsychological assessment can be combined to measure the progression of MCI and early AD. The ADNI dataset used in our experiments comprises 1728 participants from ADNI 1, 2, 3, and GO, for whom a T1w MRI was available at baseline: 339 AD, 541 CN, and 848 MCI were finally included. ADNI T1w images were performed both on 1.5T and 3T scanners with similar protocol parameters: 256×256 matrix; voxel size=1.2×1.0×1.0 mm; TI=400 ms; TR=6.98 ms; TE=2.85 ms; flip angle=11°.

These datasets are described in detail in supplementary eMethod 1. Table 1 summarizes the basic demographics of all participants from the two datasets.

**Table 1.** Summary of participant demographics for UKBB and ADNI datasets. Values for age are presented as mean  $\pm$  SD [range]. M: male, F: female.

Study	Diagnosis	Subjects	Age	Gender
UKBB	CN	4403	63.21 $\pm$ 7.41 [45, 80]	2068 M / 2335 F
	CN	541	74.02 $\pm$ 5.79 [56, 90]	253 M / 288 F
ADNI	MCI	848	73.15 $\pm$ 7.56 [54, 89]	504 M / 344 F
	AD	339	74.78 $\pm$ 7.87 [55, 90]	186 M / 153 F

### 3.2. Image preprocessing

Raw T1w MRIs were quality checked for motion, image artifacts, or restricted field-of-view. Images passing this quality check (QC) were corrected for magnetic field inhomogeneity (Tustison et al., 2010). A robust multi-atlas label fusion-based method, MUSE (Doshi et al., 2016), was applied for tissue segmentation of the brain. Voxel-wise regional volumetric maps (RAVENS) (Davatzikos et al., 2001) were generated for grey matter (GM) tissues by registering skull-stripped images to a population-based template residing in the MNI-space using a deformable registration method (Ou et al., 2011). Another QC procedure was performed to control the quality of the images further. Specifically, the images were first checked by manually evaluating for pipeline failures (e.g., poor brain extraction, tissue segmentation, and registration errors). Furthermore, a second-step automated procedure automatically flagged images based on outlying values of quantified metrics (i.e., ROI values), and those flagged images were re-evaluated.

## 4. Experiments and results

We first validated the proposed model using semi-simulated data in which we knew the ground truth for the number of clusters ( $k$ ) and subtype membership assignment. In this setting, we quantitatively assessed how several key components influenced the clustering performance and compared our method’s performance to other common clustering approaches. Finally, we applied MAGIC to a real clinical dataset for dissecting the heterogeneity of AD plus MCI.

### 4.1. Evaluation strategy

We adopted a cross-validation (CV) procedure with repeated and stratified random splits for 100 repetitions to determine the appropriate number of clusters. Specifically, during each repetition, 80% of the data was for training. The “optimal” number of clusters was guided by the clustering stability across the 100 repetitions. The Adjusted Rand index (ARI) was used for that purpose, which we denoted as ARIs during CV (ARI<sub>CV</sub>). Moreover, for simulation experiments, where the ground truth for subtype membership was known, ARI was also used to quantify the clustering performance, referred to as ARIs for ground truth (ARI<sub>GT</sub>).

After obtaining the assignment of subtype membership, we performed voxel-wise group comparisons for RAVENS GM maps between each subtype with CNs using the *3dttest++* program (Cox et al., 2017) in AFNI (Cox, 1996), to detect the distinct neuroanatomical patterns of the corresponding. The two-sample t-test T-value map of AFNI was further converted to a P-value map considering correction for multiple comparisons with the Benjamini-Hochberg procedure. Moreover, it has been advocated for reporting effect size over P-value in the

literature since P-values are highly dependent on the sample size (Sullivan and Feinn, 2012). Thus, we calculated the local effect size, Cohen's  $f^2$  (Selya et al., 2012), for voxels that are significantly different between subtypes after adjusting the confounding covariates (i.e., age and sex). We present the voxel-wise effect size maps to delineate the subtypes' neuroanatomical patterns for all experiments. For reference, Cohen's  $f^2 \geq 0.02$ ,  $\geq 0.15$ , and  $\geq 0.35$  represent small, medium, and large effect sizes, respectively (Selya et al., 2012).

## 4.2. Experiments using UKBB semi-simulated data

The UKBB RAVENS GM maps were used to generate semi-simulated data. We first divided all CN subjects ( $N=4403$ ) into pre-defined number of splits. Part of the splits were regarded as the true CN, and the remainder (i.e., pseudo-PT) was further divided into another number of splits for subtype simulations. The sample size of each subtype was balanced. Brain atrophy was then imposed to RAVENS maps of each of the subtypes within different patterns. To simplify the simulation, we assume that patterns across the  $k$  subtypes are orthogonal with each other (we further tested the influence of overlapping patterns between subtypes). These regions were priorly chosen based on the segmentation image of the template image in the MNI space. Different choices for the number of subtypes ( $k$ ) and atrophy strength level (ASL) were tested. For instance, for experiments with  $k=2$  and  $ASL=0.1$ , voxel intensity values inside the two pre-defined patterns were reduced by 10% compared to its original values. Moreover, the ASL varied by  $\pm 2\%$  across images to add randomness. In total, nine experiments were performed and summarized in Table 2. The ground truth of the pre-defined atrophy patterns of each subtype is shown in Fig. 3 (i.e., the first column).

**Table 2.** Summary of the original semi-simulated experiments. The number of subjects for each group is shown in parentheses. ASL: atrophy strength level;  $k$ : the number of clusters. Sub: Subtype.

Experiment	Subtype and sample size
$k=2$ & $ASL=0.1$	CN (2201), Sub1 (1101), Sub2 (1101)
$k=2$ & $ASL=0.2$	CN (2201), Sub1 (1101), Sub2 (1101)
$k=2$ & $ASL=0.3$	CN (2201), Sub1 (1101), Sub2 (1101)
$k=3$ & $ASL=0.1$	CN (1103), Sub1 (1100), Sub2 (1100), Sub3 (1100)
$k=3$ & $ASL=0.2$	CN (1103), Sub1 (1100), Sub2 (1100), Sub3 (1100)
$k=3$ & $ASL=0.3$	CN (1103), Sub1 (1100), Sub2 (1100), Sub3 (1100)
$k=4$ & $ASL=0.1$	CN (883), Sub1 (880), Sub2 (880), Sub3 (880), Sub4 (880)
$k=4$ & $ASL=0.2$	CN (883), Sub1 (880), Sub2 (880), Sub3 (880), Sub4 (880)
$k=4$ & $ASL=0.3$	CN (883), Sub1 (880), Sub2 (880), Sub3 (880), Sub4 (880)

The semi-simulated experiments' first aim is to compare MAGIC's clustering performance to other unsupervised or semi-supervised clustering methods. Second, the influence of confounds on clustering performance can be assessed under different conditions.

### 4.2.1. MAGIC discovers the correct number of clusters and corresponding simulated neuroanatomical patterns

MAGIC was able to discover the correct number of clusters for the following experiments:  $k=2$  &  $ASL=0.1$ , 0.2 or 0.3 (Fig. 2A, B and C),  $k=3$  &  $ASL=0.2$  (Fig. 2E) or  $ASL=0.3$  (Fig. 2F), and  $k=4$  &  $ASL=0.3$  (Fig. 2I). For other experiments, MAGIC failed to find the true  $k$  (Fig. 2D, G, and H), indicating the presence of high heterogeneity ( $K > 2$  or 3) and very subtle disease effect (10%-20%), the algorithm reaches a detection threshold.

Voxel-wise effect size maps were generated to demonstrate whether MAGIC can find the ground truth of neuroanatomical atrophy patterns of subtypes. The ground truth of neuroanatomical patterns is shown by masking out the simulated atrophy regions (i.e., the first column in Fig. 3). MAGIC was able to find the ground truth for all experiments, except for  $k=4$  &  $ASL=0.1$  (Fig. 3G), in which minor effects (Cohen's  $f^2 < 0.06$ ) were detected in subcortical structures for all four subtypes. Besides, the effect size of the subtype patterns increases with increasing ASL.

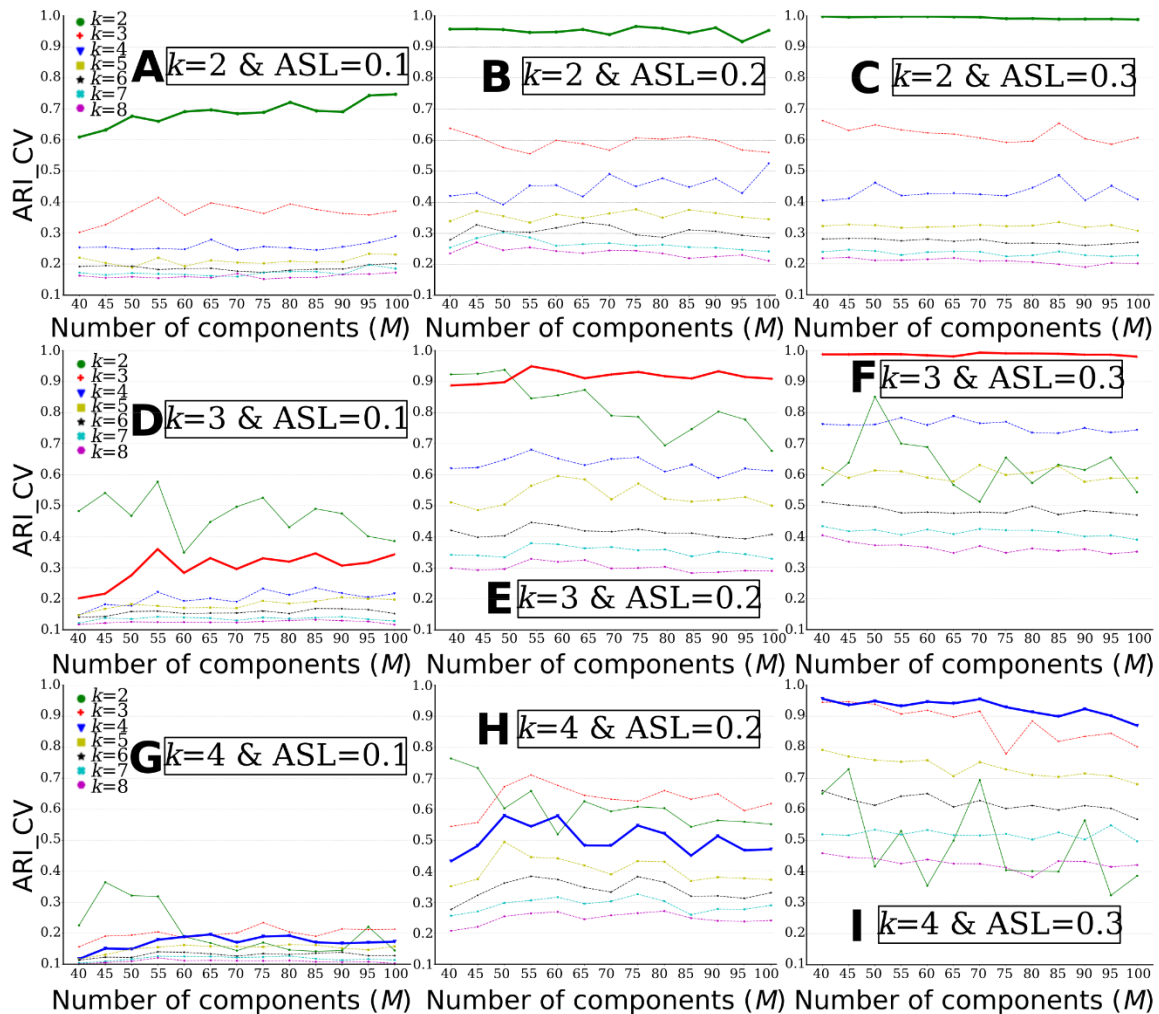


**Figure 2.** MAGIC finds the ground truth of the number of clusters ( $k$ ) when the clustering conditions are favorable, i.e., higher ASL or lower  $k$ . The “optimal”  $k$  was determined by ARI CV. A)  $k=2$  &  $ASL=0.1$ ; B)  $k=2$  &  $ASL=0.2$ ; C)  $k=2$  &  $ASL=0.3$ ; D)  $k=3$  &  $ASL=0.1$ ; E)  $k=3$  &  $ASL=0.2$ ; F)  $k=3$  &  $ASL=0.3$ ; G)  $k=4$  &  $ASL=0.1$ ; H)  $k=4$  &  $ASL=0.2$ ; I)  $k=4$  &  $ASL=0.3$ . The bold lines represent the ground truth of  $k$  for each experiment.

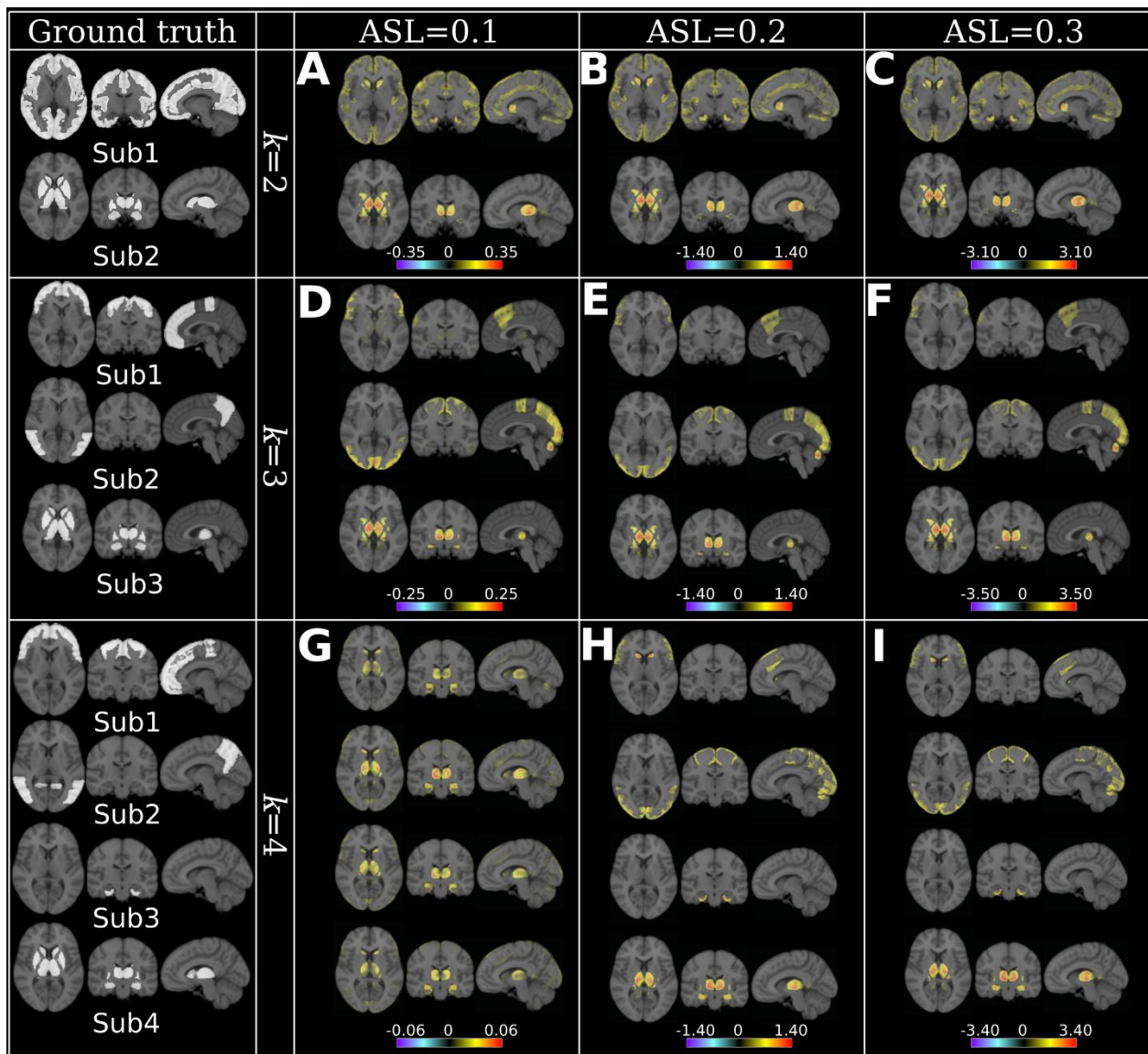


**Figure 3.** MAGIC finds the ground truth of subtype’s neuroanatomical patterns when the clustering conditions are favorable, i.e., higher ASL or lower  $k$ . Neuroanatomical patterns are displayed using effect size maps based on voxel-wise group comparisons between CN and subtypes. Positive values denote brain atrophy (CN > Sub), while negative values correspond to larger brain volume in subtypes (CN < Sub). The ground truth of the subtypes pattern is presented with a binary mask (white) for each  $k$  in the first column. Of note, as expected, due to the variances from the original data before the simulation, the ground truth and the actual patterns might not always be in concordance. For instance, for Sub in Fig A, the bilateral caudate showed smaller effect sizes, but they pass the significant threshold (0.05). A)  $k=2$  & ASL=0.1; B)  $k=2$  & ASL=0.2; C)  $k=2$  & ASL=0.3; D)  $k=3$  & ASL=0.1; E)  $k=3$  & ASL=0.2; F)  $k=3$  & ASL=0.3; G)  $k=4$  & ASL=0.1; H)  $k=4$  & ASL=0.2; I)  $k=4$  & ASL=0.3. For reference, Cohen’s  $f^2 \geq 0.02$ ,  $\geq 0.15$ , and  $\geq 0.35$  represent small, medium, and large effect sizes, respectively.

#### 4.2.2. Comparison of MAGIC to other clustering methods

We compared MAGIC to other commonly used unsupervised clustering methods and HYDRA. Specifically, K-means is a vector quantification method that aims to partition the patient population into  $k$  clusters in which each participant belongs to the cluster with the nearest mean (Hartigan and Wong, 1979). GMM performs clustering by assuming that there are specific numbers of Gaussian distributions in patients, and each of these

distributions belongs to one cluster (McLachlan and Basford, 1988). NMF aims to factorize the input matrix into two low-rank matrices with non-negative values. Intrinsically, the loading coefficient matrix conveys the clustering membership assignment (Lee and Seung, 2001). Lastly, the agglomerative hierarchical clustering (AHC) method is another unsupervised clustering method that seeks to build a hierarchy of clusters in a “bottom-up” fashion (Day and Edelsbrunner, 1984). Moreover, we fit the unsupervised methods and HYDRA with i) single-scale features (dotted curve lines in Fig. 4) and ii) multi-scale features (solid straight lines in Fig. 4) together for comprehensive comparisons, since MAGIC always take multi-scale features.

As displayed in Fig. 4, MAGIC obtained slightly better clustering results than HYDRA and substantially outperformed all other unsupervised clustering methods (i.e., K-means, GMM, NMF, and agglomerative hierarchical clustering). Specifically, MAGIC obtained higher ARI\_GT for the following experiments:  $k=2$  & ASL=0.1 (Fig. 4A),  $k=3$  & ASL=0.1 or 0.2 or 0.3 (Fig. 4D, E and F), and  $k=4$  & ASL=0.2 or 0.3 (Fig. 4H and I). All methods failed in clustering for experiment  $k=4$  & ASL=0.1 (Fig. 4G). Furthermore, fitting all multi-scale features for HYDRA did not always perform better than the single-scale features and performed worse than MAGIC. Of note, fitting all multi-scales features (i.e., 910 features) for HYDRA took a much longer time to converge the model than single-scale HYDRA or MAGIC.

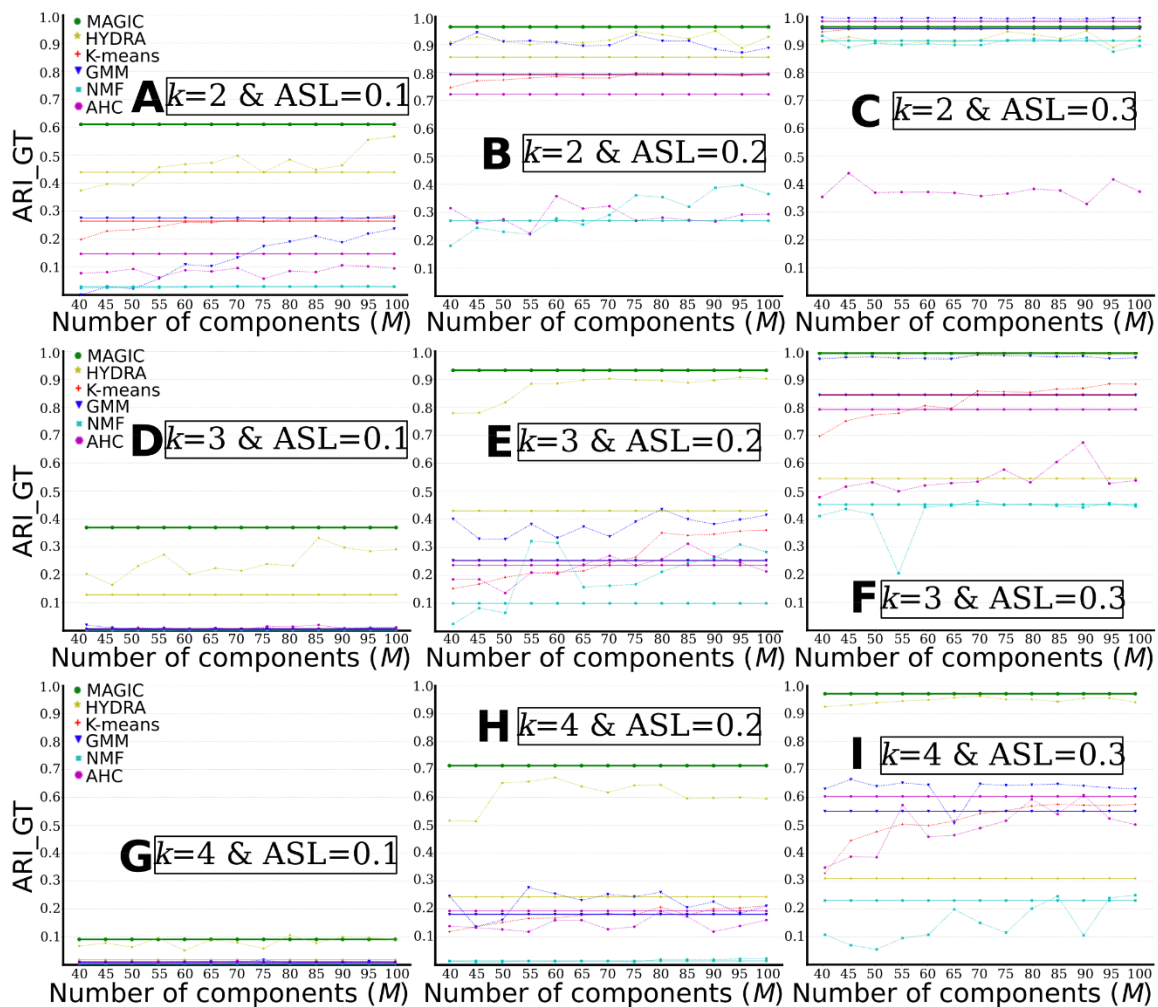


**Figure 4.** MAGIC outperforms other common clustering methods. Comparisons of clustering performance between different methods: MAGIC, HYDRA, K-means, GMM, NMF and agglomerative hierarchical clustering (AHC) ( $M=40$  to  $100$  with step as  $5$ ). The solid straight lines show clustering results for models that take multi-scale features as input and are drawn over all  $M$ s only for visualization purposes. The dotted curve lines represent clustering results for models that take single-scale features as input. A)  $k=2$  & ASL=0.1; B)  $k=2$  & ASL=0.2; C)  $k=2$  & ASL=0.3; D)  $k=3$  & ASL=0.1; E)  $k=3$  & ASL=0.2; F)  $k=3$  & ASL=0.3; G)  $k=4$  & ASL=0.1; H)  $k=4$  & ASL=0.2; I)  $k=4$  & ASL=0.3.

### 4.2.3. Influence of the number of clusters

When the number of clusters  $k$  increased, MAGIC's clustering performance gradually decreased (i.e., each column in Fig. 4 represents the three experiments with the same ASL), except for experiments  $k=4$  &  $ASL=0.3$ . For  $ASL=0.1$ , the ARI\_GTs are 0.610, 0.368 and 0.091 for  $k=2, 3$  and 4, respectively. For  $ASL=0.2$ , the ARI\_GT decreased from 0.960 to 0.934 and to 0.713 for  $k=2, 3$  and 4, respectively. For  $ASL=0.3$ , the ARI\_GTs are 0.994, 0.995 and 0.966 for  $k=2, 3$  and 4, respectively.

### 4.2.4. Influence of the atrophy strength levels

With the increase of ASL, MAGIC's clustering performance gradually improved (i.e., each row in Fig. 4 represents the three experiments with the same  $k$ ). For  $k=2$ , the ARI\_GTs are 0.610, 0.960 and 0.994 for  $ASL=0.1, 0.2$  and  $0.3$ , respectively. For  $k=3$ , the ARI\_GT increased from 0.368 to 0.934 and to 0.995 for  $ASL=0.1, 0.2$  and  $0.3$ , respectively. For  $k=4$ , the ARI\_GTs are 0.091, 0.713 and 0.966 for  $ASL=0.1, 0.2$  and  $0.3$ , respectively.

We visualized the subtypes/clusters in 2D space for all experiments using multidimensional scaling (Cox and Cox, 2008) (Fig. 5). With the increase of ASL at a given  $k$ , the clusters become more separable (i.e., each row in Fig. 5 represents the three experiments with the same  $k$ ).

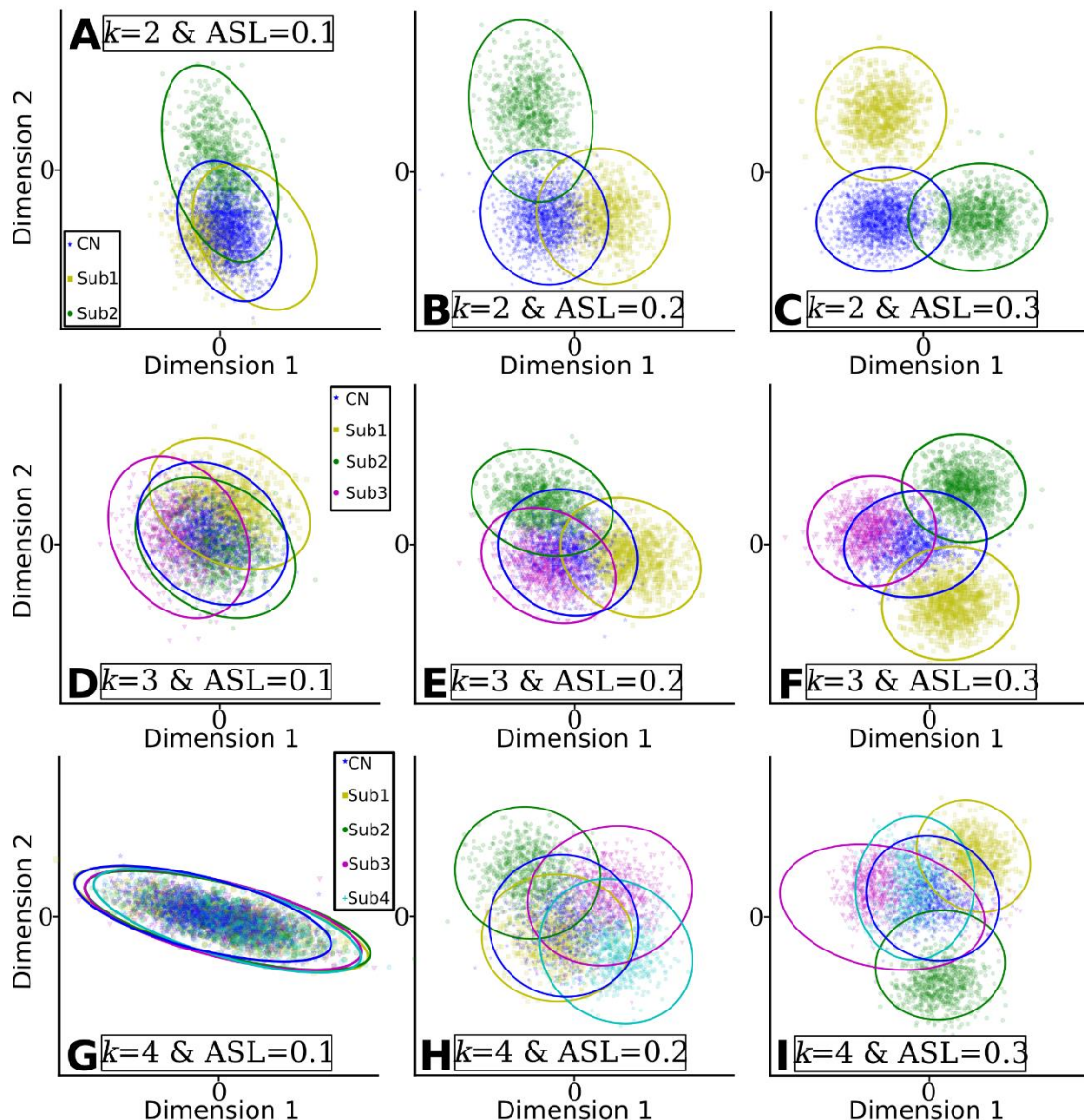




**Figure 5.** Clusters found by MAGIC become more distinguishable when the clustering conditions are favorable, i.e., higher ASL or lower  $k$ . The clusters were projected into 2D space for visualization. Dimension 1 and Dimension 2 represent the two components projected by multidimensional scaling methods. A)  $k=2$  & ASL=0.1; B)  $k=2$  & ASL=0.2; C)  $k=2$  & ASL=0.3; D)  $k=3$  & ASL=0.1; E)  $k=3$  & ASL=0.2; F)  $k=3$  & ASL=0.3; G)  $k=4$  & ASL=0.1; H)  $k=4$  & ASL=0.2; I)  $k=4$  & ASL=0.3.

#### 4.2.5. Influence of the overlapping atrophy patterns

We generated overlapping atrophy patterns based on the original experiments for each  $k$ . For  $k=2$ , Sub2 had subcortical atrophy in the initial experiments (Fig. 3), and we additionally simulated parietal atrophy. Similarly, for  $k=3$  and 4, global cortical atrophy was imposed within Sub1 (frontal atrophy subtype in the original experiments) and Sub3 (temporal atrophy subtype in the initial experiments) members, respectively. The ground truth of overlapping neuroanatomical patterns is detailed in supplementary eFigure 2.

As shown in Table 3, MAGIC obtained inferior clustering performance compared to the original experiments for i)  $k=2$  & ASL=0.1, ii)  $k=3$  & ASL=0.1, iii)  $k=3$  & ASL=0.2 and iv)  $k=4$  & ASL=0.2, and comparable results for experiments with ASL=0.3. The results for the ARI\_CV, voxel-wise effect size maps and the 2D visualization of subtypes are presented in supplementary eFigure 1, 2 and 3, respectively.

**Table 3.** Comparison of the original clustering performance (left column) to the influence of overlapping atrophy patterns (middle column) and the larger brain volume (right column). Compared to the original experiments, overlapping atrophy patterns result in lower clustering performance, while larger brain volume shows no extensive clustering performance effects.

Experiment	Original experiments	Overlapping atrophy patterns	Larger brain volume
$k=2$ & ASL=0.1	0.610	0.501	0.562
$k=2$ & ASL=0.2	0.960	0.946	0.947
$k=2$ & ASL=0.3	0.994	0.992	0.992
$k=3$ & ASL=0.1	0.368	0.281	0.393
$k=3$ & ASL=0.2	0.934	0.879	0.926
$k=3$ & ASL=0.3	0.995	0.977	0.976
$k=4$ & ASL=0.1	0.091	0.111	0.210
$k=4$ & ASL=0.2	0.713	0.628	0.731
$k=4$ & ASL=0.3	0.966	0.967	0.965

#### 4.2.6. Influence of the larger brain volume in subtypes

Instead of simulating brain atrophy as in the original experiments (Fig. 3), we introduced larger brain volumes by increasing the voxel's intensity value inside the pre-defined patterns for Sub2 members for experiments  $k=2$ , Sub3 members for experiments  $k=3$  and Sub4 members for experiments  $k=4$ . The simulated neuroanatomical patterns are detailed in supplementary eFigure 4.

As shown in Table 3, MAGIC obtained comparable clustering performance to all settings' original experiments. The results for the ARI\_CV, voxel-wise effect size maps and the 2D visualization of subtypes are presented in supplementary eFigure 4, 5, and 6, respectively.

#### 4.2.7. Influence of the data imbalance

We first evaluated the influence of data imbalance for CN vs. subtypes. The imbalance ratios were achieved by randomly subsampling from the groups of subtypes. As shown in Fig. 6 A, B, and C, clustering performance considerably increased when the groups became more balanced. With the highest imbalance ratio (8:1), all experiments obtained the lowest ARI\_GTs. Generally, the ratios of 2:1 performed on par with the ratios of 1:1 and 1:2.

We then evaluated the influence of data imbalance among subtypes by assuming that CN and PT (sum of all subtypes) were balanced (Fig. 6D, E, and F). Similarly, clustering performance considerably increased with more balanced data. On the other hand, when ASL is large (i.e., 0.3), data imbalance showed a limited impact on clustering performance (e.g., Fig. 6D and E).

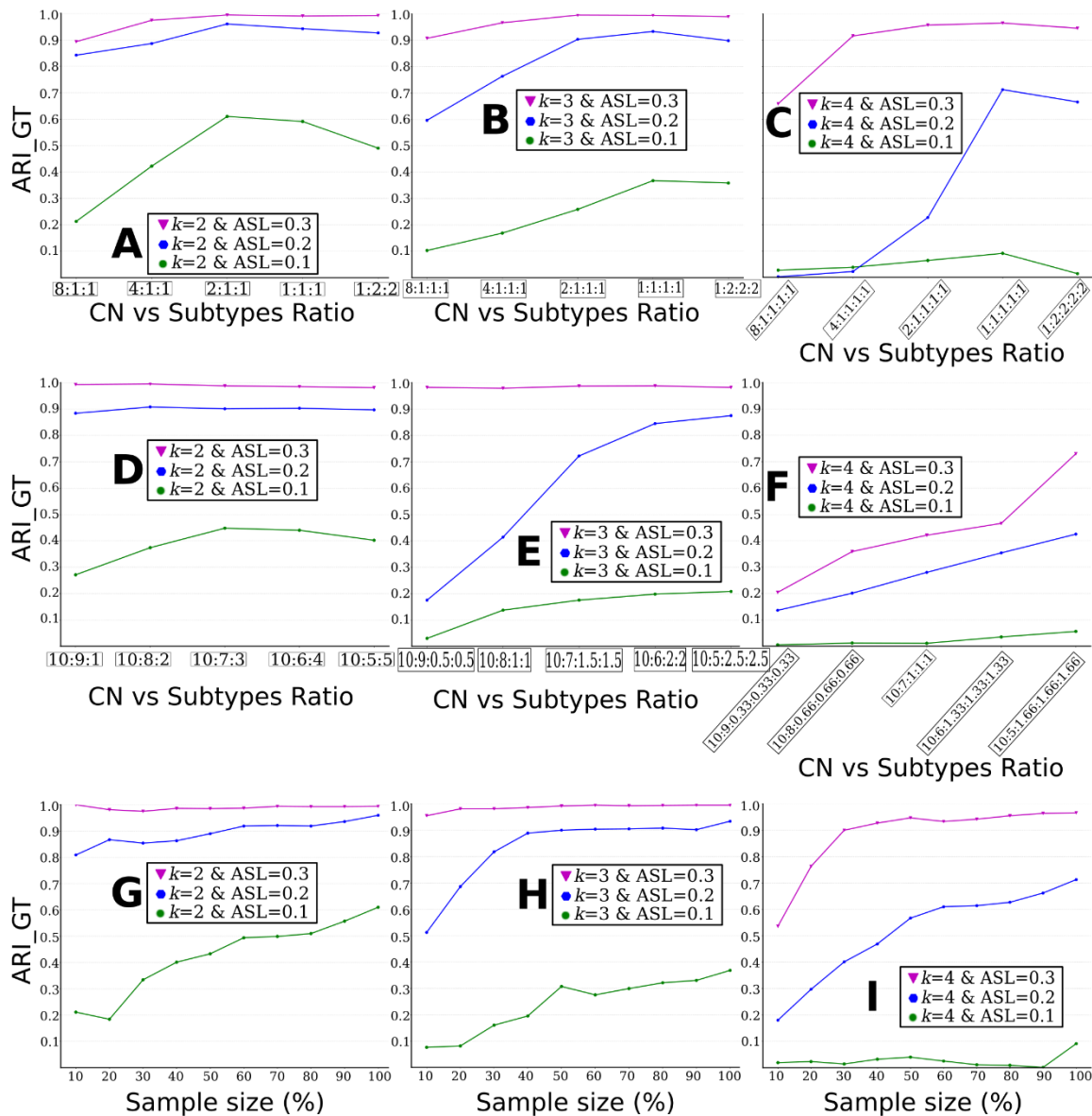


**Figure 6.** The influence of different ratios of imbalanced data between CN vs. subtypes is presented in Fig. A, B, and C, among subtypes in Fig. D, E and F. The influence of sample size is displayed in Fig. G, H, and I. A) influence of data imbalance between CN and subtypes for k=2; B) influence of data imbalance between CN and subtypes for k=3; C) influence of data imbalance between CN and subtypes for k=4; D) influence of data imbalance among subtypes for k=2. Clustering performance improves with the increase of the sample size. E)

influence of data imbalance among subtypes for  $k=3$ ; F) influence of data imbalance among subtypes for  $k=4$ ; G) influence of sample sizes for  $k=2$ ; H) influence of sample sizes for  $k=3$ ; I) influence of sample sizes for  $k=4$ .

#### 4.2.8. Influence of the sample size

The influence of the sample size on clustering performance was assessed (Fig. 6G, H and I). For each experiment, MAGIC was run with data ranging from 10% to 100% of the sample size by keeping the original group ratios unchanged (i.e., CN vs. Sub1 vs. Sub2 vs ...).

Generally, clustering performance improved with the increasing sample size. For experiments  $k=2$  &  $ASL=0.3$  and  $k=3$  &  $ASL=0.3$ , clustering performance was almost perfect at all different sample size choices. For experiment  $k=4$  &  $ASL=0.1$  (Fig. 6I), MAGIC obtained poor clustering performance.

### 4.3. Experiments using Alzheimer's disease data

When applied to ADNI data,  $ARI_{CV}$  was the highest at  $k=2$  ( $0.4 < ARI_{CV} < 0.5$ ), compared to other values of  $k$  (Fig. 7A). For  $k=2$ , The effect size maps revealed two distinct neuroanatomical patterns: i) Sub1 ( $N=396$ ) showed relatively normal brain anatomy, except for focalized brain atrophy in subcortical regions. In contrast, Sub2 ( $N=791$ ) had diffuse atrophy with the largest effect size (Cohen's  $f^2 = 0.45$ ) in the hippocampus, amygdala, and temporal regions (Fig. 7B). For  $k=3$ , the three subtypes all presented diffuse brain atrophy (Fig. 7C). For  $k=4$ , Sub1 ( $N=363$ ) preserved relatively normal brain anatomy. Sub2 ( $N=416$ ) is the typical AD pattern showing whole-brain atrophy and most severe atrophy in temporal and hippocampus regions. Sub3 ( $N=210$ ) showed atypical AD patterns without affecting the hippocampus and temporal lobes (Fig. 7D). Sub4 ( $N=198$ ) showed only focal atrophy near frontal regions. The subtype visualization in the 2D space shows that the cluster boundaries are fuzzy (Fig. 7E, F, and G). Note that we present the subtypes' neuroanatomical patterns for  $k=2$ , 3, and 4 since they each reflect latent neuroanatomical patterns at different resolutions. The solution of  $k=2$  usually divides the patients into mild and severe atrophied groups, which might not be clinically interesting. The results of  $ARI_{CV}$ , together with our semi-simulated experiments, indicate that the CV procedure may not detect the true  $k$  due to unfavorable clustering conditions (e.g., the focalized effects or small sample size).

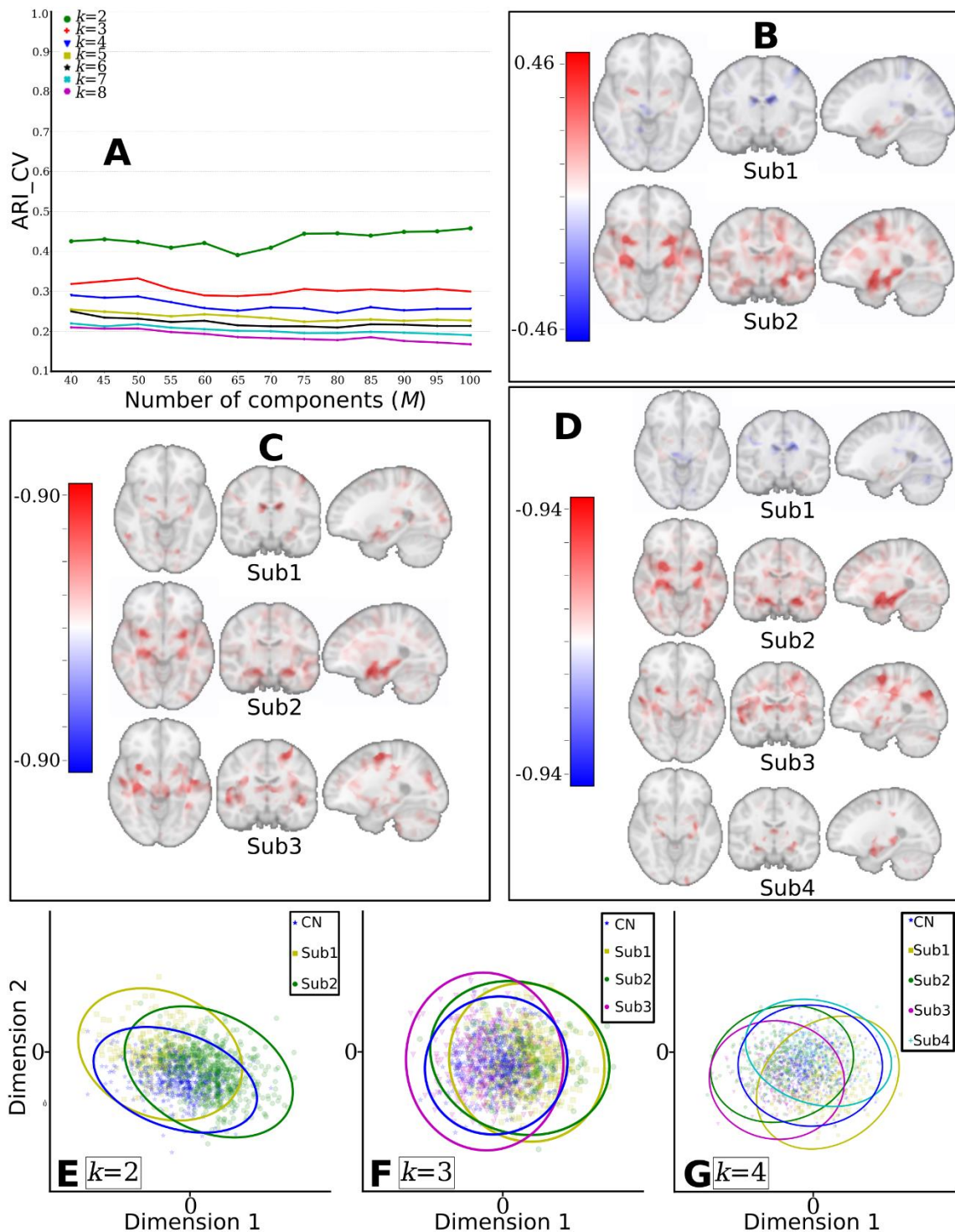


**Figure 7.** Applying MAGIC to AD and MCI patients of ADNI. We evaluated the clustering stability for different resolutions of the number of clusters and showed the subtype’s neuroanatomical patterns and the 2D visualization of the subtypes. A) Cross-validation for choosing the “optimal”  $k$ . B) Voxel-wise effect size (Cohen’s  $f_2$ ) maps for the neuroanatomical patterns between the two subtypes and CN. C) Effect size maps for the three subtypes and CN neuroanatomical patterns. D) Effect size maps for the neuroanatomical patterns between the four subtypes and CN. E) Visualization of the clusters projected to the 2D space for  $k=2$ . F) Visualization of the clusters projected to the 2D space for  $k=3$ . G) Visualization of the clusters projected to the 2D space for  $k=4$ .

## 5. Discussion

### *Synopsis*

This paper presents MAGIC, a novel multi-scale semi-supervised clustering method for dissecting disease heterogeneity. The proposed method seamlessly integrates multi-scale representation learning and semi-supervised clustering in a coherent framework via a double-cyclic optimization procedure to yield scale agnostic delineation of heterogeneous disease patterns. In contrast to existing unsupervised approaches presented in (Ezzati et al., 2020, 2020; Jeon et al., 2019, 2019; Jung et al., 2016; Lubeiro et al., 2016; Nettiksimmons et al., 2014; Ota et al., 2016; Pan et al., 2020; Park et al., 2017; Planchuelo-Gómez et al., 2020; Poulakis et al., 2020, 2020, 2018; Sugihara et al., 2016; Ten Kate et al., 2018), MAGIC is a semi-supervised approach, leveraging the patient-control dichotomy to drive subtypes that reflect distinct pathological processes. In contrast to the existing state-of-the-art semi-supervised clustering method (i.e., HYDRA), MAGIC can accurately delineate effect patterns that are both global and focal, thanks to its multi-scale optimization routine. The validity of MAGIC is demonstrated in semi-simulated experiments. We show MAGIC's ability to discern disease subtypes and their neuroanatomical patterns under various simulated scenarios constructed by varying the ASL, sample size, and sample imbalance, respectively. Subsequently, we applied MAGIC to AD plus MCI to disentangle their neuroanatomical heterogeneity, demonstrating the potential of MAGIC in real large neuroimaging studies, as well as our insights in interpreting the claimed subtypes.

### *MAGIC outperforms comparable heterogeneity analysis methods*

Concerning clustering performance, MAGIC outperformed competing methods. On the one hand, compared to HYDRA, the minor gain in clustering accuracy in MAGIC is likely driven by multi-scale features that can better explain the variance due to heterogeneity. We hypothesize that the opNMF multi-scale components accurately reflect multi-scale brain organization that has previously been demonstrated in network analysis (Betzler and Bassett, 2017), brain modeling (Schirner et al., 2018), and signal processing (Starck et al., 1998) in the literature. Furthermore, multi-scale learning has shown great potential in medical imaging for different tasks, such as segmentation (Doshi et al., 2016; Kamnitsas et al., 2017) or classification (Cui et al., 2016; Hu et al., 2016). On the other hand, MAGIC substantially outperforms unsupervised clustering methods. Since unsupervised clustering methods directly partition patient samples into clusters based on similarity/dissimilarity or distance (Altman and Krzywinski, 2017), they may be more likely driven by confounding factors such as brain size, age, and sex instead of pathology-related variations, which is partially addressed by MAGIC. Namely, MAGIC can derive pathology-driven subtypes in a multi-scale manner by leveraging the reference label (i.e., CN) and the fuzzy patient labels (i.e., PT).

### *Under what conditions does MAGIC succeed or fail?*

The critical yet challenging choice to be made in all algorithms related to clustering is to choose the appropriate number of clusters (Climescu-Haulica, 2007; Fu and Perry, 2020; Mirkin, 2011) since all clustering methods find patterns in data - whether they are real or not (Altman and Krzywinski, 2017). In addition to providing a new clustering method, we provided guidelines to these heterogeneity analysis algorithms' practitioners. Specifically, our experiments shed light on selecting the number of clusters and provide criteria when the clustering analysis is reliable and when it needs to be approached with caution. In general, we suggest performing model selection using a cross-validation strategy based on clustering stability. In our experiments, ARI reliably recovered the ground truth number of clusters when the ASL and sample size were large and data was reasonably balanced. However, one should note that a lower number of clusters intrinsically gives more stable results (i.e., higher ARI<sub>CV</sub>). In such cases, in actual clinical applications, other insights may be required to support further the subtypes found, such as the effect size map or prior clinical knowledge.

Different choices of the key components (e.g., sample size or data imbalance) have detrimental or positive influences on clustering. With the increase of the complexity of clustering (e.g., increasing the number of clusters or decreasing ASL), MAGIC's clustering performance degrades gradually. This is to be expected as the boundaries between clusters become increasingly blurred and indivisible. Moreover, imbalanced data have adverse effects on clustering results. This is in line with previous findings (Dubey et al., 2014; Samper-González et al., 2018). The authors found that balanced data obtained better classification results than the imbalanced using T1w MRI from ADNI. To note, MAGIC essentially performs clustering and supervised classification simultaneously. Unsurprisingly, increased sample size leads to better clustering performance, consistent with

the findings from previous studies (Abdulkadir et al., 2011; Chu et al., 2011; Franke et al., 2010; Samper-González et al., 2018; Schulz et al., 2020). The rule of thumb in semi-supervised clustering is to collect moderately balanced data and large samples in practice. Finally, instead of larger brain patterns, adding overlapping patterns made it more difficult to disentangle these effects. The former situation is more commonly present in practice. In these cases, larger sample cohorts may be needed to unravel the overlapping heterogeneity.

Our semi-simulated experiments are of great value for assessing clustering results. They enable us to understand potential false-positive results. Namely, suppose the sample size, ARI\_CV, and/or the effect sizes are low. In that case, none of the existing methods may uncover the true heterogeneity or may reveal a lower number of subtypes than what is present.

### *Subtypes of AD and MCI share overlapping neuroanatomical patterns*

Applying the proposed method to structural imaging data from ADNI resulted in subtypes that share overlapping neuroanatomical patterns. The model selection indicated the “optimal” number of clusters as  $k=2$  (ARI\_CV<0.5). However, this stratification generally clusters the patients into mild and severe atrophy patterns, which is not clinically interesting. Here, we focused on the four-subtype resolution since this was consistent with previous findings (Dong et al., 2016b; Yang et al., 2020), in which the study population is similar to ours.

Among these subtypes, Sub1 and Sub4 display normal brain anatomy (Fig. 7D). This was supported by the distribution of AD/MCI in these subtypes. Sub1 (278 MCI & 85 AD) and Sub4 (164 MCI & 34 AD) have the highest proportion of MCI. The normal anatomy subtype has been confirmed in previous works (Dong et al., 2016b; Ezzati et al., 2020; Jung et al., 2016; Nettiksimmons et al., 2014; Ota et al., 2016; Poulakis et al., 2020, 2018; Ten Kate et al., 2018; Yang et al., 2020). In (Dong et al., 2016b), the authors examined the external validation of the subtypes. They demonstrated that the normal-like subtype had the lowest frequency with abnormal CSF amyloid-b 1-42 levels, normal CSF-tau levels, most minor baseline cognitive impairment, and slowest rates of cognitive decline. Sub2 showed typical AD-like neuroanatomical patterns with diffuse atrophy over the whole brain, with the largest effect size in the hippocampus and medial temporal lobe. Those affected regions have been widely reported as hallmarks of AD in case-control studies (Hanyu et al., 1998; Müller et al., 2005; Varghese et al., 2013) and have been confirmed in previous clustering literature (Dong et al., 2016b; Nettiksimmons et al., 2014; Noh et al., 2014; Poulakis et al., 2018; Ten Kate et al., 2018; Varol et al., 2017; Yang et al., 2020; Young et al., 2018). Conversely, Sub3 showed an atypical widespread atrophy pattern that did not include the hippocampus and the temporal lobe (Dong et al., 2016b; Poulakis et al., 2018; Yang et al., 2020). Despite the methodological difference across studies, the resulting subtypes’ agreement emphasizes that AD should be considered a neuroanatomically heterogeneous disease. These distinct imaging signatures or dimensions may elucidate different brain mechanisms and pathways leading to AD.

### *Potential and challenges*

The application of clustering methods to neuroimaging data has recently drawn significant attention and has led to several key publications in recent years. Herein we demonstrated MAGIC’s potential for dissecting the neuroanatomical heterogeneity of brain diseases, indicating that the current “all-in-one-bucket” diagnostic criteria may not be appropriate for certain neurodegenerative and neuropsychiatric disorders. On the other hand, clustering methods always end up with clusters, even if there are no natural clusters in the data (Altman and Krzywinski, 2017). If they indeed exist, the disease subtypes often present neuroanatomically overlapping patterns, unlike the semi-simulated conditions with purely defined orthogonal patterns. None of the heterogeneity analysis tools were sufficiently powered to accurately disentangle heterogeneity in small sample cohorts or with weak discriminative power of pattern identifiability in our experiments. In this case, care must be taken to provide additional information, such as external validation of subtypes to clinical profiles, to substantiate any clinical interpretation of the identified subtypes.

Furthermore, the reproducibility of clustering, effect size maps of subtypes, and sample imbalance should be carefully examined. Ultimately, good practices, such as extensive reproducibility analyses, including permutation tests (Chand et al., 2020), should be performed to support the subtypes’ stability and robustness. However, we observed a steady improvement of clustering performance with increased sample sizes even with overlapping anatomical patterns. This is a promising sign for the utility of these machine learning-based clustering tools with the increasing presence of large neuroimaging consortia.

Our model nevertheless has the following limitations. First, MAGIC is designed for “pure” clustering tasks that seek the disease’s subtypes without considering the disease progression factors or stages (Young et al., 2018). A future direction is extending MAGIC to assign subtypes to longitudinal scans and study the diseases’ progression. Moreover, the sample size of AD necessary to draw a solid conclusion for those subtypes may be larger than analyzed. Clustering performance was positively associated with sample size in our simulation. Lastly, a possible extension of the proposed method is integrating clinical or genetic data to derive subtypes that show consistency across different modalities.

## Acknowledgements

This work was granted access to be supported in part by NIH grants R01MH112070, 1U01AG068057, 1RF1AG054409, and R01AG067103. Data collection and sharing for this project was funded by the Alzheimer's Disease Neuroimaging Initiative (ADNI) (National Institutes of Health Grant U01 AG024904) and DOD ADNI (Department of Defense award number W81XWH-12-2-0012). ADNI is funded by the National Institute on Aging, the National Institute of Biomedical Imaging and Bioengineering, and through generous contributions from the following: AbbVie, Alzheimer's Association; Alzheimer's Drug Discovery Foundation; Araclon Biotech; BioClinica, Inc.; Biogen; Bristol-Myers Squibb Company; CereSpir, Inc.; Cogstate; Eisai Inc.; Elan Pharmaceuticals, Inc.; Eli Lilly and Company; EuroImmun; F. Hoffmann-La Roche Ltd and its affiliated company Genentech, Inc.; Fujirebio; GE Healthcare; IXICO Ltd.; Janssen Alzheimer Immunotherapy Research & Development, LLC.; Johnson & Johnson Pharmaceutical Research & Development LLC.; Lumosity; Lundbeck; Merck & Co., Inc.; Meso Scale Diagnostics, LLC.; NeuroRx Research; Neurotrack Technologies; Novartis Pharmaceuticals Corporation; Pfizer Inc.; Piramal Imaging; Servier; Takeda Pharmaceutical Company; and Transition Therapeutics. The Canadian Institutes of Health Research is providing funds to support ADNI clinical sites in Canada. Private sector contributions are facilitated by the Foundation for the National Institutes of Health ([www.fnih.org](http://www.fnih.org)). The grantee organization is the Northern California Institute for Research and Education, and the study is coordinated by the Alzheimer's Therapeutic Research Institute at the University of Southern California. ADNI data are disseminated by the Laboratory for Neuro Imaging at the University of Southern California. This research has also been conducted using the UK Biobank Resource (UKBB Application Number: 35148): <https://www.ukbiobank.ac.uk/>.



## References

- Abdulkadir, A., Mortamet, B., Vemuri, P., Jack, C.R., Krueger, G., Klöppel, S., Alzheimer's Disease Neuroimaging Initiative, 2011. Effects of hardware heterogeneity on the performance of SVM Alzheimer's disease classifier. *Neuroimage* 58, 785–792. <https://doi.org/10.1016/j.neuroimage.2011.06.029>
- Aisen, P.S., Petersen, R.C., Donohue, M.C., Gamst, A., Raman, R., Thomas, R.G., Walter, S., Trojanowski, J.Q., Shaw, L.M., Beckett, L.A., Jack, C.R., Jr, Jagust, W., Toga, A.W., Saykin, A.J., Morris, J.C., Green, R.C., Weiner, M.W., Alzheimer's Disease Neuroimaging Initiative, 2010. Clinical Core of the Alzheimer's Disease Neuroimaging Initiative: progress and plans. *Alzheimers. Dement.* 6, 239–246.
- Altman, N., Krzywinski, M., 2017. Clustering. *Nat Methods* 14, 545–546. <https://doi.org/10.1038/nmeth.4299>
- Ashburner, J., Friston, K.J., 2000. Voxel-based morphometry--the methods. *Neuroimage* 11, 805–821. <https://doi.org/10.1006/nimg.2000.0582>
- Ashburner, J., Hutton, C., Frackowiak, R., Johnsrude, I., Price, C., Friston, K., 1998. Identifying global anatomical differences: deformation-based morphometry. *Hum Brain Mapp* 6, 348–357.
- Bashyam, V.M., Erus, G., Doshi, J., Habes, M., Nasrallah, I.M., Truelove-Hill, M., Srinivasan, D., Mamourian, L., Pomponio, R., Fan, Y., Launer, L.J., Masters, C.L., Maruff, P., Zhuo, C., Völzke, H., Johnson, S.C., Fripp, J., Koutsouleris, N., Satterthwaite, T.D., Wolf, D., Gur, R.E., Gur, R.C., Morris, J., Albert, M.S., Grabe, H.J., Resnick, S., Bryan, R.N., Wolk, D.A., Shou, H., Davatzikos, C., on behalf of the ISTAGING Consortium, the P.A. disease C., ADNI, and CARDIA studies, 2020. MRI signatures of brain age and disease over the lifespan based on a deep brain network and 14 468 individuals worldwide. *Brain* 143, 2312–2324. <https://doi.org/10.1093/brain/awaa160>
- Bassett, D.S., Siebenhühner, F., 2013. Multiscale Network Organization in the Human Brain, in: *Multiscale Analysis and Nonlinear Dynamics*. John Wiley & Sons, Ltd, pp. 179–204. <https://doi.org/10.1002/9783527671632.ch07>
- Betzal, R.F., Bassett, D.S., 2017. Multi-scale brain networks. *NeuroImage, Functional Architecture of the Brain* 160, 73–83. <https://doi.org/10.1016/j.neuroimage.2016.11.006>
- Chand, G.B., Dwyer, D.B., Erus, G., Sotiras, A., Varol, E., Srinivasan, D., Doshi, J., Pomponio, R., Pignoni, A., Dazzan, P., Kahn, R.S., Schnack, H.G., Zanetti, M.V., Meisenzahl, E., Busatto, G.F., Crespo-Facorro, B., Pantelis, C., Wood, S.J., Zhuo, C., Shinohara, R.T., Shou, H., Fan, Y., Gur, R.C., Gur, R.E., Satterthwaite, T.D., Koutsouleris, N., Wolf, D.H., Davatzikos, C., 2020. Two distinct neuroanatomical subtypes of schizophrenia revealed using machine learning. *Brain* 143, 1027–1038. <https://doi.org/10.1093/brain/awaa025>
- Chang, C.-C., Lin, C.-J., 2011. LIBSVM: A library for support vector machines. *ACM Trans. Intell. Syst. Technol.* 2, 1–27. <https://doi.org/10.1145/1961189.1961199>
- Chu, C., Hsu, A.-L., Chou, K.-H., Bandettini, P.A., Lin, C., Initiative, A.D.N., 2011. Does feature selection improve classification accuracy? Impact of sample size and feature selection on classification using anatomical magnetic resonance images [WWW Document]. *NeuroImage*. <https://doi.org/10.1016/j.neuroimage.2011.11.066>
- Climescu-Haulica, A., 2007. How to Choose the Number of Clusters: The Cramer Multiplicity Solution, in: Decker, R., Lenz, H.-J. (Eds.), *Advances in Data Analysis, Studies in Classification, Data Analysis, and Knowledge Organization*. Springer, Berlin, Heidelberg, pp. 15–22. [https://doi.org/10.1007/978-3-540-70981-7\\_2](https://doi.org/10.1007/978-3-540-70981-7_2)
- Cox, M.A.A., Cox, T.F., 2008. Multidimensional Scaling, in: Chen, C., Härdle, W., Unwin, A. (Eds.), *Handbook of Data Visualization, Springer Handbooks Comp.Statistics*. Springer, Berlin, Heidelberg, pp. 315–347. [https://doi.org/10.1007/978-3-540-33037-0\\_14](https://doi.org/10.1007/978-3-540-33037-0_14)

- Cox, R.W., 1996. AFNI: software for analysis and visualization of functional magnetic resonance neuroimages. *Comput. Biomed. Res.* 29, 162–173.
- Cox, R.W., Chen, G., Glen, D.R., Reynolds, R.C., Taylor, P.A., 2017. fMRI clustering and false-positive rates. *Proc Natl Acad Sci U S A* 114, E3370–E3371. <https://doi.org/10.1073/pnas.1614961114>
- Cui, Z., Chen, W., Chen, Y., 2016. Multi-Scale Convolutional Neural Networks for Time Series Classification. *ArXiv*.
- Cuingnet, R., Gerardin, E., Tessieras, J., Auzias, G., Lehéricy, S., Habert, M.-O., Chupin, M., Benali, H., Colliot, O., 2011. Automatic classification of patients with Alzheimer’s disease from structural MRI: A comparison of ten methods using the ADNI database. *NeuroImage* 56, 766–781. <https://doi.org/10.1016/j.neuroimage.2010.06.013>
- Davatzikos, C., 2019. Machine learning in neuroimaging: Progress and challenges. *NeuroImage* 197, 652–656. <https://doi.org/10.1016/j.neuroimage.2018.10.003>
- Davatzikos, C., Genc, A., Xu, D., Resnick, S.M., 2001. Voxel-based morphometry using the RAVENS maps: methods and validation using simulated longitudinal atrophy. *Neuroimage* 14, 1361–1369. <https://doi.org/10.1006/nimg.2001.0937>
- Day, W.H.E., Edelsbrunner, H., 1984. Efficient algorithms for agglomerative hierarchical clustering methods. *Journal of Classification* 1, 7–24. <https://doi.org/10.1007/BF01890115>
- Dong, A., Honnorat, N., Gaonkar, B., Davatzikos, C., 2016a. CHIMERA: Clustering of Heterogeneous Disease Effects via Distribution Matching of Imaging Patterns. *IEEE Trans. Med. Imaging* 35, 612–621. <https://doi.org/10.1109/TMI.2015.2487423>
- Dong, A., Toledo, J.B., Honnorat, N., Doshi, J., Varol, E., Sotiras, A., Wolk, D., Trojanowski, J.Q., Davatzikos, C., for the Alzheimer’s Disease Neuroimaging Initiative, 2016b. Heterogeneity of neuroanatomical patterns in prodromal Alzheimer’s disease: links to cognition, progression and biomarkers. *Brain* aww319. <https://doi.org/10.1093/brain/aww319>
- Doshi, J., Erus, G., Ou, Y., Resnick, S.M., Gur, R.C., Gur, R.E., Satterthwaite, T.D., Furth, S., Davatzikos, C., Alzheimer’s Neuroimaging Initiative, 2016. MUSE: MUlti-atlas region Segmentation utilizing Ensembles of registration algorithms and parameters, and locally optimal atlas selection. *Neuroimage* 127, 186–195. <https://doi.org/10.1016/j.neuroimage.2015.11.073>
- Dubey, R., Zhou, J., Wang, Y., Thompson, P.M., Ye, J., 2014. ANALYSIS OF SAMPLING TECHNIQUES FOR IMBALANCED DATA: AN N=648 ADNI STUDY. *Neuroimage* 87, 220–241. <https://doi.org/10.1016/j.neuroimage.2013.10.005>
- Dwyer, D.B., Cabral, C., Kambeitz-Ilanovic, L., Sanfelici, R., Kambeitz, J., Calhoun, V., Falkai, P., Pantelis, C., Meisenzahl, E., Koutsouleris, N., 2018. Brain Subtyping Enhances The Neuroanatomical Discrimination of Schizophrenia. *Schizophrenia Bulletin* 44, 1060–1069. <https://doi.org/10.1093/schbul/sby008>
- Ecker, C., Rocha-Rego, V., Johnston, P., Mourao-Miranda, J., Marquand, A., Daly, E.M., Brammer, M.J., Murphy, C., Murphy, D.G., MRC AIMS Consortium, 2010. Investigating the predictive value of whole-brain structural MR scans in autism: a pattern classification approach. *Neuroimage* 49, 44–56. <https://doi.org/10.1016/j.neuroimage.2009.08.024>
- Ezzati, A., Ezzati, A., Zammit, A.R., Habeck, C., Hall, C.B., Lipton, R.B., 2020. Detecting biological heterogeneity patterns in ADNI amnesic mild cognitive impairment based on volumetric MRI. *Brain Imaging and Behavior* 14, 1792–1804. <https://doi.org/10.1007/s11682-019-00115-6>
- Filipovych, R., Resnick, S.M., Davatzikos, C., 2012. JointMMCC: Joint Maximum-Margin Classification and Clustering of Imaging Data. *IEEE Trans. Med. Imaging* 31, 1124–1140. <https://doi.org/10.1109/TMI.2012.2186977>

- Franke, K., Ziegler, G., Klöppel, S., Gaser, C., Alzheimer's Disease Neuroimaging Initiative, 2010. Estimating the age of healthy subjects from T1-weighted MRI scans using kernel methods: exploring the influence of various parameters. *Neuroimage* 50, 883–892. <https://doi.org/10.1016/j.neuroimage.2010.01.005>
- Friston, K.J., Holmes, A.P., Worsley, K.J., Poline, J.-P., Frith, C.D., Frackowiak, R.S.J., 1994. Statistical parametric maps in functional imaging: A general linear approach. *Human Brain Mapping* 2, 189–210. <https://doi.org/10.1002/hbm.460020402>
- Fu, W., Perry, P.O., 2020. Estimating the Number of Clusters Using Cross-Validation. *Journal of Computational and Graphical Statistics* 29, 162–173. <https://doi.org/10.1080/10618600.2019.1647846>
- Gaonkar, B., Davatzikos, C., 2013. Analytic estimation of statistical significance maps for support vector machine based multi-variate image analysis and classification. *NeuroImage* 78, 270–283. <https://doi.org/10.1016/j.neuroimage.2013.03.066>
- Habes, M., Janowitz, D., Erus, G., Toledo, J.B., Resnick, S.M., Doshi, J., Van der Auwera, S., Wittfeld, K., Hegenscheid, K., Hosten, N., Biffar, R., Homuth, G., Völzke, H., Grabe, H.J., Hoffmann, W., Davatzikos, C., 2016. Advanced brain aging: relationship with epidemiologic and genetic risk factors, and overlap with Alzheimer disease atrophy patterns. *Transl Psychiatry* 6, e775–e775. <https://doi.org/10.1038/tp.2016.39>
- Hanyu, H., Sakurai, H., Iwamoto, T., Takasaki, M., Shindo, H., Abe, K., 1998. Diffusion-weighted MR imaging of the hippocampus and temporal white matter in Alzheimer's disease. *J. Neurol. Sci.* 156, 195–200.
- Hartigan, J.A., Wong, M.A., 1979. Algorithm AS 136: A K-Means Clustering Algorithm. *Journal of the Royal Statistical Society. Series C (Applied Statistics)* 28, 100–108. <https://doi.org/10.2307/2346830>
- Honorat, N., Dong, A., Meisenzahl-Lechner, E., Koutsouleris, N., Davatzikos, C., 2019. Neuroanatomical heterogeneity of schizophrenia revealed by semi-supervised machine learning methods. *Schizophrenia Research* 214, 43–50. <https://doi.org/10.1016/j.schres.2017.12.008>
- Hu, K., Wang, Y., Chen, K., Hou, L., Zhang, X., 2016. Multi-scale features extraction from baseline structure MRI for MCI patient classification and AD early diagnosis. *Neurocomputing* 175, 132–145. <https://doi.org/10.1016/j.neucom.2015.10.043>
- Insel, T.R., Cuthbert, B.N., 2015. Brain disorders? Precisely. *Science* 348, 499–500. <https://doi.org/10.1126/science.aab2358>
- Jeon, S., Kang, J.M., Seo, S., Jeong, H.J., Funck, T., Lee, S.-Y., Park, K.H., Lee, Y.-B., Yeon, B.K., Ido, T., Okamura, N., Evans, A.C., Na, D.L., Noh, Y., 2019. Topographical Heterogeneity of Alzheimer's Disease Based on MR Imaging, Tau PET, and Amyloid PET. *Front. Aging Neurosci.* 11, 211. <https://doi.org/10.3389/fnagi.2019.00211>
- Jung, N.-Y., Seo, S.W., Yoo, H., Yang, J.-J., Park, S., Kim, Y.J., Lee, J., Lee, J.S., Jang, Y.K., Lee, J.M., Kim, S.T., Kim, S., Kim, E.-J., Na, D.L., Kim, H.J., 2016. Classifying anatomical subtypes of subjective memory impairment. *Neurobiology of Aging* 48, 53–60. <https://doi.org/10.1016/j.neurobiolaging.2016.08.010>
- Kamnitsas, K., Ledig, C., Newcombe, V., Simpson, J., Kane, A.D., Menon, D., Rueckert, D., Glocker, B., 2017. Efficient multi-scale 3D CNN with fully connected CRF for accurate brain lesion segmentation. *Medical Image Anal.* <https://doi.org/10.1016/j.media.2016.10.004>
- Koutsouleris, N., Meisenzahl, E.M., Borgwardt, S., Riecher-Rössler, A., Frodl, T., Kambeitz, J., Köhler, Y., Falkai, P., Möller, H.-J., Reiser, M., Davatzikos, C., 2015. Individualized differential diagnosis of schizophrenia and mood disorders using neuroanatomical biomarkers. *Brain* 138, 2059–2073. <https://doi.org/10.1093/brain/awv111>
- Lao, Z., Shen, D., Xue, Z., Karacali, B., Resnick, S.M., Davatzikos, C., 2004. Morphological classification of brains via high-dimensional shape transformations and machine learning methods. *NeuroImage* 21, 46–57. <https://doi.org/10.1016/j.neuroimage.2003.09.027>

- Lee, D.D., Seung, H.S., 2001. Algorithms for Non-negative Matrix Factorization 7.
- Lubeiro, A., Rueda, C., Hernández, J.A., Sanz, J., Sarramea, F., Molina, V., 2016. Identification of two clusters within schizophrenia with different structural, functional and clinical characteristics. *Progress in Neuro-Psychopharmacology and Biological Psychiatry* 64, 79–86. <https://doi.org/10.1016/j.pnpbp.2015.06.015>
- McLachlan, G.J., Basford, K.E., 1988. *Mixture Models: Inference And Applications To Clustering* 1.
- Miller, K.L., Alfaro-Almagro, F., Bangerter, N.K., Thomas, D.L., Yacoub, E., Xu, J., Bartsch, A.J., Jbabdi, S., Sotiropoulos, S.N., Andersson, J.L., Griffanti, L., Douaud, G., Okell, T.W., Weale, P., Dragonu, I., Garratt, S., Hudson, S., Collins, R., Jenkinson, M., Matthews, P.M., Smith, S.M., 2016. Multimodal population brain imaging in the UK Biobank prospective epidemiological study. *Nat Neurosci* 19, 1523–1536. <https://doi.org/10.1038/nn.4393>
- Miotto, R., Wang, F., Wang, S., Jiang, X., Dudley, J.T., 2018. Deep learning for healthcare: review, opportunities and challenges. *Briefings in Bioinformatics* 19, 1236–1246. <https://doi.org/10.1093/bib/bbx044>
- Mirkin, B., 2011. Choosing the number of clusters. *WIREs Data Mining Knowl Discov* 1, 252–260. <https://doi.org/10.1002/widm.15>
- Müller, M.J., Greverus, D., Dellani, P.R., Weibrich, C., Wille, P.R., Scheurich, A., Stoeter, P., Fellgiebel, A., 2005. Functional implications of hippocampal volume and diffusivity in mild cognitive impairment. *Neuroimage* 28, 1033–1042.
- Murray, M.E., Graff-Radford, N.R., Ross, O.A., Petersen, R.C., Duara, R., Dickson, D.W., 2011. Neuropathologically defined subtypes of Alzheimer’s disease with distinct clinical characteristics: a retrospective study. *The Lancet Neurology* 10, 785–796. [https://doi.org/10.1016/S1474-4422\(11\)70156-9](https://doi.org/10.1016/S1474-4422(11)70156-9)
- Nettiksimmons, J., DeCarli, C., Landau, S., Beckett, L., 2014. Biological heterogeneity in ADNI amnesic mild cognitive impairment. *Alzheimer’s & Dementia* 10, 511–521.e1. <https://doi.org/10.1016/j.jalz.2013.09.003>
- Ng, A.Y., Jordan, M.I., Weiss, Y., 2001. On Spectral Clustering: Analysis and an algorithm, in: *Advances in Neural Information Processing Systems*. MIT Press, pp. 849–856.
- Noh, Y., Jeon, S., Lee, J.M., Seo, S.W., Kim, G.H., Cho, H., Ye, B.S., Yoon, C.W., Kim, H.J., Chin, J., Park, K.H., Heilman, K.M., Na, D.L., 2014. Anatomical heterogeneity of Alzheimer disease: Based on cortical thickness on MRIs. *Neurology* 83, 1936–1944. <https://doi.org/10.1212/WNL.0000000000001003>
- Ota, K., for the Alzheimer’s Disease Neuroimaging Initiative, Ota, K., Oishi, N., Ito, K., Fukuyama, H., 2016. Prediction of Alzheimer’s Disease in Amnesic Mild Cognitive Impairment Subtypes: Stratification Based on Imaging Biomarkers. *JAD* 52, 1385–1401. <https://doi.org/10.3233/JAD-160145>
- Ou, Y., Sotiras, A., Paragios, N., Davatzikos, C., 2011. DRAMMS: Deformable Registration via Attribute Matching and Mutual-Saliency Weighting. *Med Image Anal* 15, 622–639. <https://doi.org/10.1016/j.media.2010.07.002>
- Pan, Y., Pu, W., Chen, X., Huang, X., Cai, Y., Tao, H., Xue, Z., Mackinley, M., Limongi, R., Liu, Z., Palaniyappan, L., 2020. Morphological Profiling of Schizophrenia: Cluster Analysis of MRI-Based Cortical Thickness Data. *Schizophrenia Bulletin* 46, 623–632. <https://doi.org/10.1093/schbul/sbz112>
- Park, J.-Y., Park, J.-Y., Na, H.K., Kim, S., Kim, H., Kim, H.J., Seo, S.W., Na, D.L., Han, C.E., Seong, J.-K., 2017. Robust Identification of Alzheimer’s Disease subtypes based on cortical atrophy patterns. *Sci Rep* 7, 43270. <https://doi.org/10.1038/srep43270>

- Petersen, R.C., Aisen, P.S., Beckett, L.A., Donohue, M.C., Gamst, A.C., Harvey, D.J., Jack, C.R., Jr, Jagust, W.J., Shaw, L.M., Toga, A.W., Trojanowski, J.Q., Weiner, M.W., 2010. Alzheimer's Disease Neuroimaging Initiative (ADNI): clinical characterization. *Neurology* 74, 201–209.
- Planchuelo-Gómez, Á., Lubeiro, A., Núñez-Novo, P., Gomez-Pilar, J., de Luis-García, R., del Valle, P., Martín-Santiago, Ó., Pérez-Escudero, A., Molina, V., 2020. Identificación of MRI-based psychosis subtypes: Replication and refinement. *Progress in Neuro-Psychopharmacology and Biological Psychiatry* 100, 109907. <https://doi.org/10.1016/j.pnpbp.2020.109907>
- Poulakis, K., Ferreira, D., Pereira, J.B., Smedby, Ö., Vemuri, P., Westman, E., 2020. Fully bayesian longitudinal unsupervised learning for the assessment and visualization of AD heterogeneity and progression 26.
- Poulakis, K., Pereira, J.B., Mecocci, P., Vellas, B., Tsolaki, M., Kłoszewska, I., Soininen, H., Lovestone, S., Simmons, A., Wahlund, L.-O., Westman, E., 2018. Heterogeneous patterns of brain atrophy in Alzheimer's disease. *Neurobiology of Aging* 65, 98–108. <https://doi.org/10.1016/j.neurobiolaging.2018.01.009>
- Rathore, S., Habes, M., Iftikhar, M.A., Shacklett, A., Davatzikos, C., 2017. A review on neuroimaging-based classification studies and associated feature extraction methods for Alzheimer's disease and its prodromal stages. *Neuroimage* 155, 530–548.
- Samper-González, J., Burgos, N., Bottani, S., Fontanella, S., Lu, P., Marcoux, A., Routier, A., Guillon, J., Bacci, M., Wen, J., Bertrand, A., Bertin, H., Habert, M.-O., Durrleman, S., Evgeniou, T., Colliot, O., 2018. Reproducible evaluation of classification methods in Alzheimer's disease: Framework and application to MRI and PET data. *NeuroImage* 183, 504–521. <https://doi.org/10.1016/j.neuroimage.2018.08.042>
- Schirner, M., McIntosh, A.R., Jirsa, V., Deco, G., Ritter, P., 2018. Inferring multi-scale neural mechanisms with brain network modelling. *eLife* 7, e28927. <https://doi.org/10.7554/eLife.28927>
- Schulz, M.-A., Yeo, B.T.T., Vogelstein, J.T., Mourao-Miranada, J., Kather, J.N., Kording, K., Richards, B., Bzdok, D., 2020. Different scaling of linear models and deep learning in UKBiobank brain images versus machine-learning datasets. *Nat Commun* 11, 4238. <https://doi.org/10.1038/s41467-020-18037-z>
- Selya, A.S., Rose, J.S., Dierker, L.C., Hedeker, D., Mermelstein, R.J., 2012. A Practical Guide to Calculating Cohen's  $f^2$ , a Measure of Local Effect Size, from PROC MIXED. *Front Psychol* 3. <https://doi.org/10.3389/fpsyg.2012.00111>
- Sotiras, A., Resnick, S.M., Davatzikos, C., 2015. Finding imaging patterns of structural covariance via Non-Negative Matrix Factorization. *NeuroImage* 108, 1–16. <https://doi.org/10.1016/j.neuroimage.2014.11.045>
- Starck, J.-L., Murtagh, F., Bijaoui, A., 1998. *Image Processing and Data Analysis - The Multiscale Approach*. <https://doi.org/10.1017/CBO9780511564352>
- Sugihara, G., Oishi, N., Son, S., Kubota, M., Takahashi, H., Murai, T., 2016. Distinct Patterns of Cerebral Cortical Thinning in Schizophrenia: A Neuroimaging Data-Driven Approach. *SCHBUL sbw176*. <https://doi.org/10.1093/schbul/sbw176>
- Ten Kate, M., Dicks, E., Visser, P.J., van der Flier, W.M., Teunissen, C.E., Barkhof, F., Scheltens, P., Tijms, B.M., Alzheimer's Disease Neuroimaging Initiative, 2018. Atrophy subtypes in prodromal Alzheimer's disease are associated with cognitive decline. *Brain* 141, 3443–3456. <https://doi.org/10.1093/brain/awy264>
- Tustison, N.J., Avants, B.B., Cook, P.A., Zheng, Y., Egan, A., Yushkevich, P.A., Gee, J.C., 2010. N4ITK: improved N3 bias correction. *IEEE Trans. Med. Imaging* 29, 1310–1320.
- Varghese, T., Sheelakumari, R., James, J.S., Mathuranath, P., 2013. A review of neuroimaging biomarkers of Alzheimer's disease. *Neurol Asia* 18, 239–248.
- Varol, E., Sotiras, A., Davatzikos, C., 2018. MIDAS: Regionally linear multivariate discriminative statistical mapping. *NeuroImage* 174, 111–126. <https://doi.org/10.1016/j.neuroimage.2018.02.060>

- Varol, E., Sotiras, A., Davatzikos, C., 2017. HYDRA: Revealing heterogeneity of imaging and genetic patterns through a multiple max-margin discriminative analysis framework. *NeuroImage* 145, 346–364. <https://doi.org/10.1016/j.neuroimage.2016.02.041>
- Wen, J., Thibeau-Sutre, E., Diaz-Melo, M., Samper-González, J., Routier, A., Bottani, S., Dormont, D., Durrleman, S., Burgos, N., Colliot, O., 2020a. Convolutional neural networks for classification of Alzheimer’s disease: Overview and reproducible evaluation. *Medical Image Analysis* 63, 101694. <https://doi.org/10.1016/j.media.2020.101694>
- Wen, J., Varol, E., Chand, G., Sotiras, A., Davatzikos, C., 2020b. MAGIC: Multi-scale Heterogeneity Analysis and Clustering for Brain Diseases, in: Martel, A.L., Abolmaesumi, P., Stoyanov, D., Mateus, D., Zuluaga, M.A., Zhou, S.K., Racoceanu, D., Joskowicz, L. (Eds.), *Medical Image Computing and Computer Assisted Intervention – MICCAI 2020, Lecture Notes in Computer Science*. Springer International Publishing, Cham, pp. 678–687. [https://doi.org/10.1007/978-3-030-59728-3\\_66](https://doi.org/10.1007/978-3-030-59728-3_66)
- Whitwell, J.L., Petersen, R.C., Negash, S., Weigand, S.D., Kantarci, K., Ivnik, R.J., Knopman, D.S., Boeve, B.F., Smith, G.E., Jack, C.R., 2007. Patterns of Atrophy differ among Specific Subtypes of Mild Cognitive Impairment. *Arch Neurol* 64, 1130–1138. <https://doi.org/10.1001/archneur.64.8.1130>
- Yang, Z., Wen, J., Davatzikos, C., 2020. Smile-GANs: Semi-supervised clustering via GANs for dissecting brain disease heterogeneity from medical images. *arXiv:2006.15255* [cs, eess, q-bio, stat].
- Young, A.L., The Alzheimer’s Disease Neuroimaging Initiative (ADNI), Young, A.L., Marinescu, R.V., Oxtoby, N.P., Bocchetta, M., Yong, K., Firth, N.C., Cash, D.M., Thomas, D.L., Dick, K.M., Cardoso, J., van Swieten, J., Borroni, B., Galimberti, D., Masellis, M., Tartaglia, M.C., Rowe, J.B., Graff, C., Tagliavini, F., Frisoni, G.B., Laforce, R., Finger, E., de Mendonça, A., Sorbi, S., Warren, J.D., Crutch, S., Fox, N.C., Ourselin, S., Schott, J.M., Rohrer, J.D., Alexander, D.C., 2018. Uncovering the heterogeneity and temporal complexity of neurodegenerative diseases with Subtype and Stage Inference. *Nat Commun* 9, 4273. <https://doi.org/10.1038/s41467-018-05892-0>
- Zhang, X., Mormino, E.C., Sun, N., Sperling, R.A., Sabuncu, M.R., Yeo, B.T.T., the Alzheimer’s Disease Neuroimaging Initiative, 2016. Bayesian model reveals latent atrophy factors with dissociable cognitive trajectories in Alzheimer’s disease. *Proc Natl Acad Sci USA* 113, E6535–E6544. <https://doi.org/10.1073/pnas.1611073113>
- Zhirong Yang, Oja, E., 2010. Linear and Nonlinear Projective Nonnegative Matrix Factorization. *IEEE Trans. Neural Netw.* 21, 734–749. <https://doi.org/10.1109/TNN.2010.2041361>